LITHIUM IONIC CONDUCTIVITY AND STABILITY OF CUBIC $Li_7La_3Zr_2O_{12}$ SOLID ELECTROLYTE: A FIRST-PRINCIPLES STUDY

A Thesis
Submitted to the Graduate Faculty
of the
North Dakota State University
of Agriculture and Applied Science

By

Sudipto Saha

In Partial Fulfillment of the Requirements
for the Degree of
MASTER OF SCIENCE

Major Department:
Electrical and Computer Engineering

December 2019

Fargo, North Dakota

North Dakota State University
Graduate School

Title

LITHIUM IONIC CONDUCTIVITY AND STABILITY OF CUBIC $Li_7La_3Zr_2O_{12}$ SOLID ELECTROLYTE : A FIRST-PRINCIPLES STUDY

By

Sudipto Saha

The Supervisory Committee certifies that this ***disquisition*** complies with North Dakota State University's regulations and meets the accepted standards for the degree of

MASTER OF SCIENCE

SUPERVISORY COMMITTEE:

Dr. Qifeng Zhang
Chair

Dr. Jacob Glower

Dr. Dmitri Kilin

Dr. Khang Hoang

Approved:

April 22, 2020
Date

Dr. Benjamin Braaten
Department Chair

ABSTRACT

Garnet structured cubic LLZO crystal ($Li_{56}La_{24}Zr_{16}O_{96}$) is one of the most promising solid electrolytes for next-generation solid-state lithium-ion batteries. *Ab initio* molecular dynamics simulations have been employed to study the impacts of lithium vacancy defect and doping concentration on the lithium ionic conductivity and stability of LLZO. The number of lithium atoms in a unit cell of LLZO has been reduced from 56 to 53, where 56 lithium atoms represent the structure of stoichiometric LLZO, i.e., $Li_7La_3Zr_2O_{12}$. Similarly, the effect of Al and Ga doping on the conductivity and stability of LLZO material was also investigated. Our computational results confirm that both the defects help in enhancing the conductivity of LLZO and the concentration of defect introduced controls the trade-off between the conductivity and stability. Overall, this study provides a valuable insight into the enhancement of conductivity of cubic LLZO garnet material along with structural stability.

ACKNOWLEDGEMENTS

The accomplishment of this dissertation would not have been possible at all without the help and support of many people. First, I would like to express my deepest gratitude to my supervisor Dr. Qifeng Zhang for the chance to work on an exciting research topic and for his support and guidance with patience. I would like to thank the ECE department and CCAST of North Dakota State University for providing an ideal environment for my graduate studies here.

For the nice time at North Dakota State University, I like to appreciate all my colleagues and friends. I am greatly thankful to my lab mates – Pingchun Guo, Michael Johnson and Ama Obinna. They were always there to support me during my hard times. I would also like to thank Ashiq Adnan, Md Razuan Hossain, and Dipankar Mitra for their support and assistance during my NDSU journey.

Most importantly, none of this would have been possible without the assistance of Shafiqul Islam Shaolin. He gave me a constant support and guidance in each and every single step of my DFT calculations. Research aside, the most important things I learned from him are: how to pick important scientific questions, how to think critically, and how to get insights from computation and modeling. I would also thank Al Arabi because of his brilliant support with the python codes and thoughtful responses. I enjoyed the discussions with them, and I appreciate all the help they offered me during the past two years.

I also want to thank Dr. Hoang Khang and Dr. Dmitri Kilin. I learnt a lot from them during the interactions. The dissertation would not have been possible without the advice from these outstanding researchers.

Special thanks to my parents for all the support, understanding, and accompany, which gives me the courage to pursue my dream. I would love to thank my mother, especially, for her

unconditional love and support throughout my whole life. I appreciate the sacrifice she has made for me. Nothing would have been possible without the patience and encouragement of my mother.

Finally, a very special thanks goes to my beautiful wife, Monica for her constant love and support. There are no words to describe my gratitude. She has always been the closest to me even though we are in two different parts of the world. You are more than a friend.

I will be forever indebted to your kindness.

Thank you.

DEDICATION

I dedicate this thesis to my beloved parents,

Santosh Kumar Saha & Kanika Saha.

TABLE OF CONTENTS

LIST OF TABLES

LIST OF FIGURES

LIST OF APPENDIX TABLES

1. INTRODUCTION

1.1. Motivation

Rechargeable lithium-ion batteries are now widely used in the energy storing devices, electric vehicles, and portable electronics [1]–[5]. Higher volumetric and gravimetric energy density compared with other battery technologies have made the extensive use of Li-ion batteries in diversified fields from the electrification of transportations to the support of smart grids. To accelerate this paradigm of lithium-ion batteries, optimization in the energy density has been highly focused. Improving the electrode properties, for example, by raising the voltage of cathodes and increasing the capacity of anodes [1], [2] have been focused on the optimization of Li-ion systems. However, the flammability and toxicity of organic liquid electrolytes result in safety issues limiting their further development in larger stationary energy storage systems [6], [7]. Replacing conventional electrolytes with an inorganic solid electrolyte, which can prevent thermal runaway in case of battery failure, is of utmost importance to improve the safety and reliability of current Li-ion batteries [8]. Moreover, in the case of solid-state electrolytes, metallic Li can be used as the negative electrode, resulting in batteries with a high voltage, high energy density, and longer life-cycle. A compelling solid-state electrolyte has the potentiality to open hundreds of opportunities for high-capacity battery concepts shown in Figure 1.1 [3].

In addition to the advantages mentioned above, some solids have a wide electrochemical window that enables the use of high voltage cathodes. The high voltage cathodes offer an additional gain in energy density [9]. Carbonate based liquid electrolytes typically have electrochemical windows beyond 4.3 V that enable oxidative decomposition at that voltage [9], [10]. Solid electrolytes with a window grater than 5 V have been employed for high energy density cathodes [11].

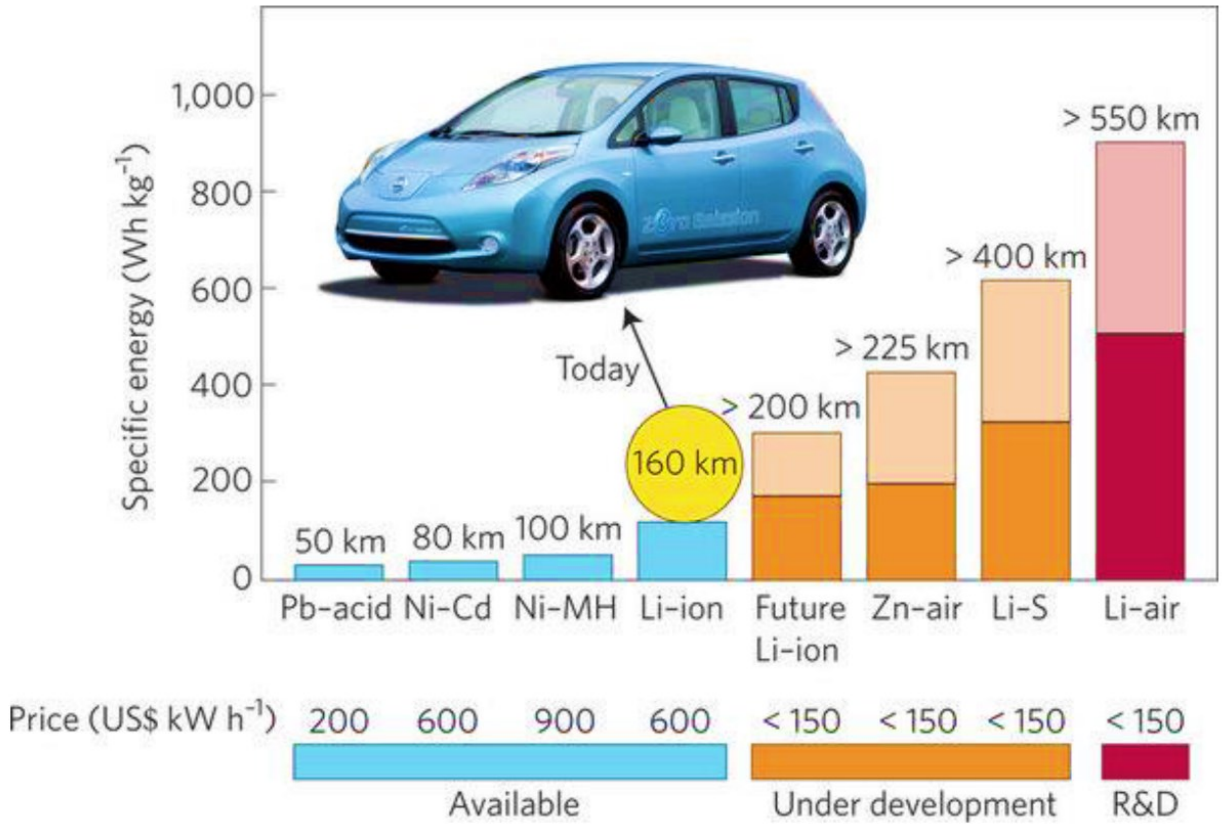

Figure 1.1. Specific energy for existing and developmental batteries along with estimated driving distances and pack prices. Taken from Bruce et al. [3].

1.2. Solid Electrolytes

For a practical application in Li-ion batteries, electrolyte materials need to satisfy several strict criteria simultaneously: high ionic conductivity, low electronic conductivity, chemical compatibility with electrodes, a wide electrochemical operating voltage, environmentally benign, and simple manufacturing process [12]. A number of classes of lithium compounds such as perovskites [8], NASICON-like [13], LISICON-like [14], garnets [15], and argyrodite [16] have been identified as solid electrolytes. Figure 1.2 shows several categories of solid electrolytes [17] developed in the last decades. However, almost all of them can only partially satisfy the requirements listed above. For instance, sulfide ions have higher polarizability than the oxide ions. For that reason, sulfide materials exhibit higher ionic conductivities than oxides [18]. For example,

$Li_{10}GeP_2S_{12}$ (LGPS) has high conductivity, up to 12 mS/cm, and is stable for a wide operating voltage range [19], [20], which is comparable to conventional liquid electrolytes [19]. However, sulfides are hygroscopic, and it may rapidly decompose to toxic H_2S gas while exposing to water [21]. On the contrary, oxides are generally highly stable against air and easy to handle.

Among the Lithium-ion conducting oxides, NaSICON type solid electrolyte has been reported as a compound with high conductivity. For instance, $Li_{1.3}Al_{0.3}Ti_{1.7}(PO_4)_3$ exhibit as high as ~10^{-3} S/cm [22], [23]. However, this material is unstable in contact with lithium [24]. Similarly, though LIPON appears to be stable for a wide stability window, its room temperature conductivity is as low as ~10^{-6} S/cm, and its fabrication requires expensive thin-film vapor deposition equipment[25]. Perovskites also show high conductivity in the range of 0.1-1 mS/cm [22], [26]. Nevertheless, like NaSICON, they are also unstable in contact with Li [17], [22], [26] and exhibit high grain boundary resistance.

To date, garnet-type lithium-ion electrolytes appear as the most promising class of solid material that may meet most of the requirements mentioned above [27]. Among garnet-type electrolytes, $Li_7La_3Zr_2O_{12}$ (LLZO) has been regarded as the most promising candidate because of its stability with elemental lithium [28], high Li-ion conductivity [29], [30], and wide electrochemical operation window [28], [31].

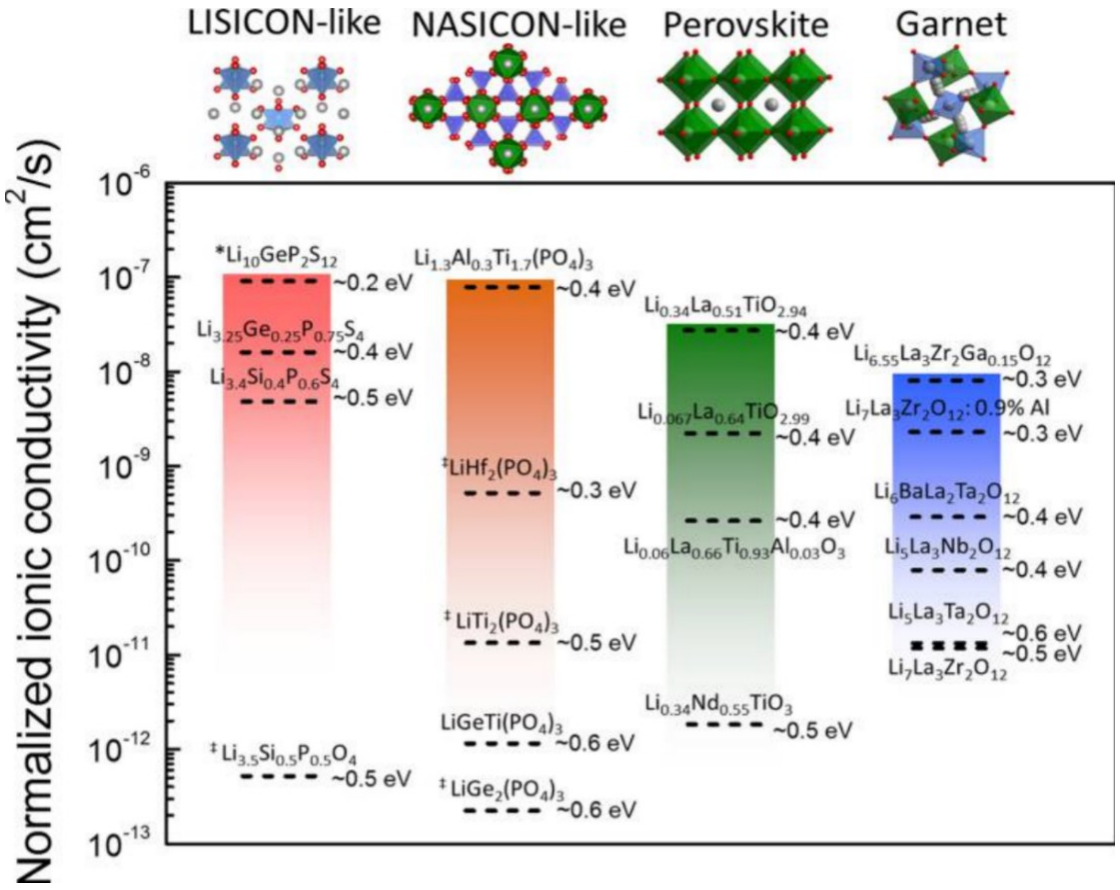

Figure 1.2. Normalized ionic conductivities and activation energies at room temperature of different lithium-ion conductors. Adapted from Bachman et al. [17].

1.3. $Li_7La_3Zr_2O_{12}$ (LLZO)

The garnet types electrolytes represent a family of complex oxide compounds spanning a broad range of compositions [32], [33]. The garnet-type compound LLZO was first identified as a lithium-ion conductor by Thangadurai and Murugan in 2007 [32]. LLZO has two different polymorphs: tetragonal structure [space group $I4_1/acd$] and cubic structure [space group $Ia\bar{3}d$] [34][34], [35]. The tetragonal structure is poor in Li-ion conduction (~10^{-6} S/cm at room temperature) because the Li-ions are stabilized in low energy sites, and all the Li sites are fully occupied by lithium ions. Unlike the tetragonal structure, cubic LLZO has a higher degree of disorder and is much more conductive [36]. The reported conductivity of cubic LLZO structure at

room temperature [37] is on the order of ~10^{-4} S/cm, which is about two orders of magnitude higher than that of the tetragonal structure (~10^{-6} S/cm) [34], [38].

The garnet structure $A_3B_3C_2O_{12}$ is comprised of a $B_3C_2O_{12}$ framework of B cations in 8-coordination sites and C cations in the octahedral sites [39]. The lithium migration pathways consist of tetrahedral sites and octahedral sites, and it depends on the three-dimensional interstitial space within the framework [40]. Compared to the general garnet structure, $A_3B_3C_2O_{12}$, $Li_7La_3Zr_2O_{12}$ has additional Li-ions "jammed" into the interstitial space in LLZO [41]–[43] that results in the Li occupancy of octahedral sites. Figure 1.3 shows the lithium sublattice of the two polymorphs of LLZO. Both the tetragonal and cubic structures of garnet LLZO have a unit cell ($Li_{56}La_{24}Zr_{16}O_{96}$) containing eight formula units ($Li_7La_3Zr_2O_{12}$). Both the structures have La and Zr ions located in the center of LaO_8 dodecahedrons and ZrO_6 octahedrons, respectively. O ions fully occupy the 96h sites in both the structures. The tetragonal LLZO is an ordered structure with lithium fully occupying the 8a (8 Li atoms), 16f (16Li atoms), and 32g sites (32 Li atoms), [36], [44]. In other words, tetragonal LLZO (8 formula units) contains 56 lithium atoms in the unit cell. On the contrary, the cubic LLZO is disordered with 24d tetrahedral and 96h octahedral sites partially occupied by lithium ions [12], [37], [45]. 56 Li atoms of LLZO (8 formula units) are distributed amongst the partially occupied 24d and 96h lithium sites in the cubic LLZO. This occupancy of Li sites makes the cubic structure significantly different from the tetragonal one.

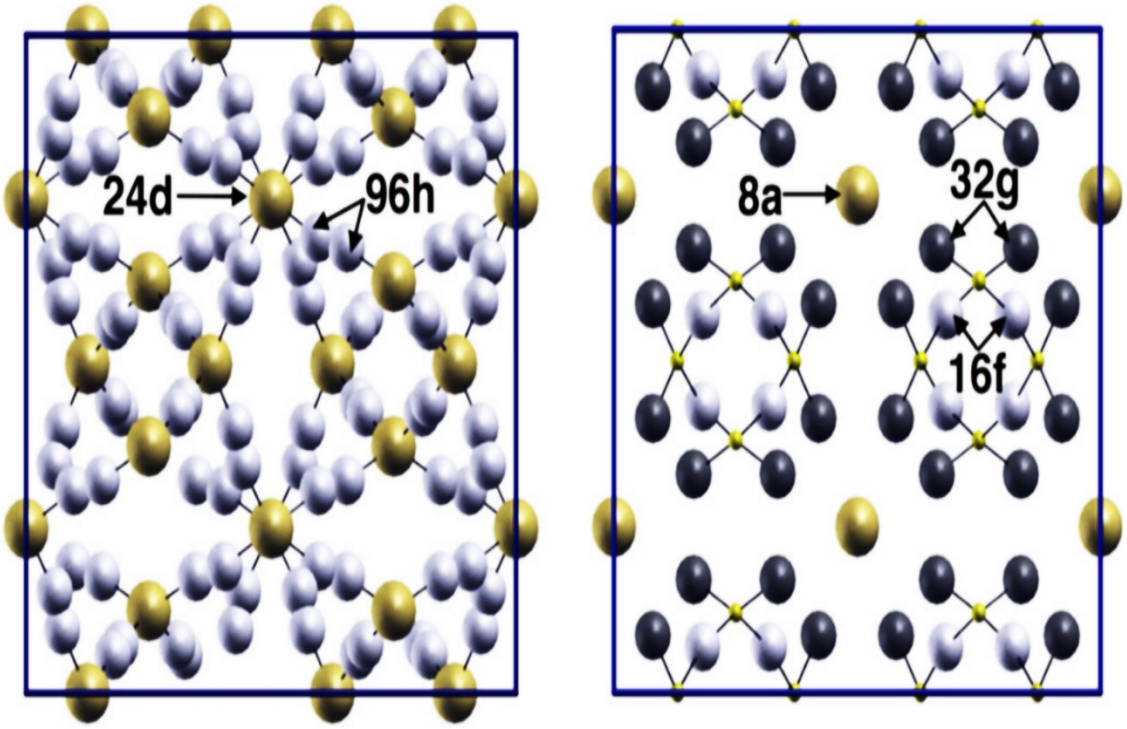

Figure 1.3. Li sublattice for the cubic (left) and tetragonal (right) phases of LLZO. Taken from Bernstein et al. [38].

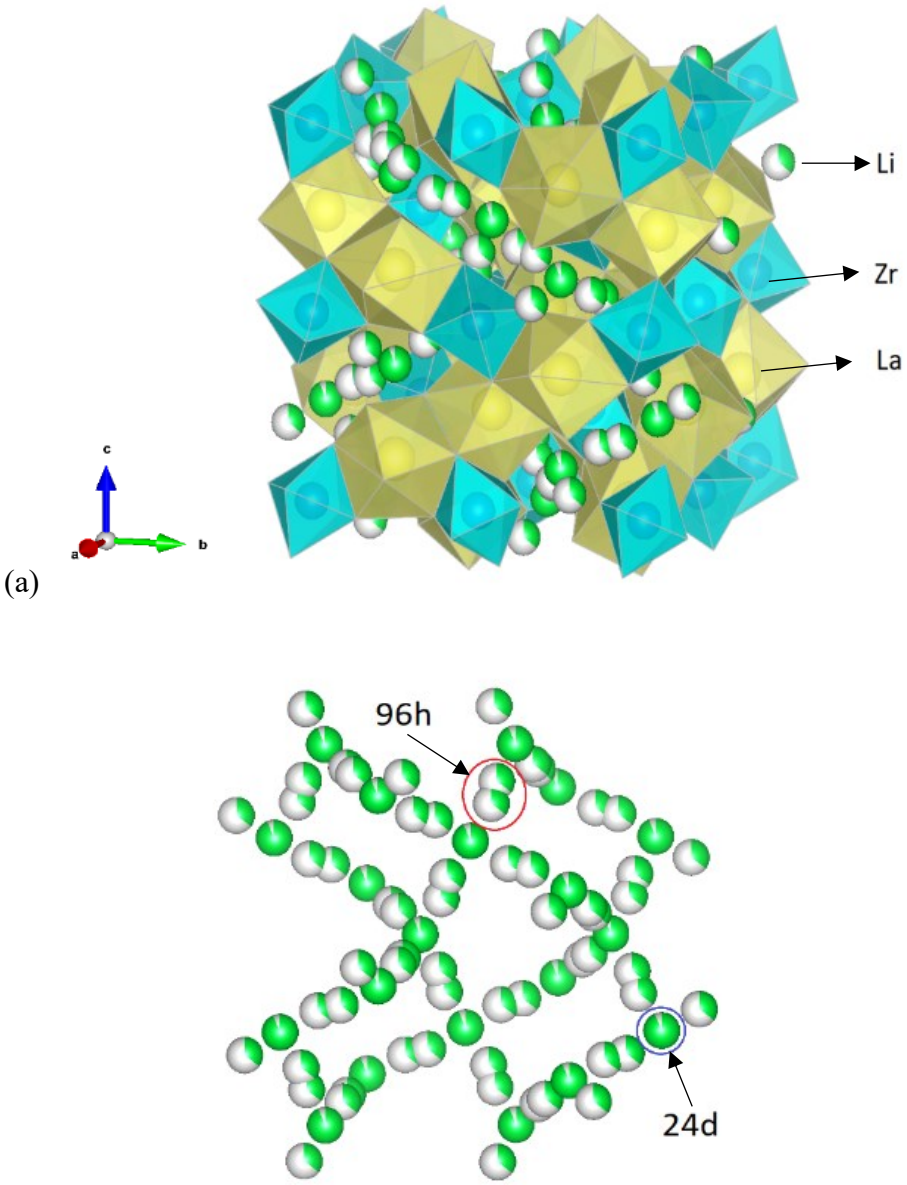

Figure 1.4. (a) Crystal structure of garnet cubic $Li_7La_3Zr_2O_{12}$ with space group $Ia\bar{3}d$. Li-ions are represented by partially filled spheres, indicating partial occupancy. La and Zr ions are in the center of yellow dodecahedrons and blue octahedrons, respectively. (b) The Li-ion diffusion pathway, comprising 24d tetrahedral sites (white/dark-green spheres) coordinated by 96h octahedral sites (white/light green spheres).

The structure of pristine cubic LLZO is shown in figure 1.4. We obtained the initial disordered structure from the ICSD (CC: 422259). It is worth noting that the obtained cubic

structure contains excess Li sites because of the partial occupation of lithium atoms in 24d and 96h sites (Figure 1.4).

There has been some research about the influences of defects and doping on the lithium ionic conductivity of LLZO. In 2011, H. Buschmann et al. reported tetragonal LLZO material with conductivity and activation energy 2.3×10^{-6} S/cm and 0.49, respectively, which is two orders of magnitude lower room temperature conductivity than the cubic LLZO electrolyte with Al-doping [46]. In the next year, J Wolfenstine et al. improved the conductivity of tetragonal LLZO to 2.3×10^{-5} S/cm hot-pressing to near theoretical density [47]. The formation of defects is an important factor in controlling the chemical stability of battery materials, and therefore, the formation of energy has been performed for a variety of materials such as Li_2S, Na_2O, Na_2CO_3, $LiMO_2$ (M = Co, Ni, Mn) and Li_2CO_3. Defect chemistry in c-LLZO has been only investigated considering adding or removing Li ions into Li sites using DFT calculations by KC et al. [48]. However, the stability range of c-LLZO and other possible defect types such as vacant have not been considered by KC et al. [46]. Zhan et al. recently performed the formation of complex defects of Li^+ and O^{2-} vacancies in cubic LLZO using XPS, AC impedance, and DC polarization measurements [49]. Here, we performed a theoretical study of defect chemistry in cubic LLZO.

1.4. Goals and Outline

The thesis deals with the investigation of the conductivity and structural stability properties of LLZO at the atomic scale. This approach helps to develop the fundamental understanding of the impact of lithium vacancy and doping on the total ionic conductivity and stability of cubic LLZO. This study aims to investigate the impacts of the lithium vacancy density and the dopant concentration on the ionic conductivity and structural stability of cubic LLZO material using first-principles-based computation. Removing lithium atoms from a unit cell adopted as $Li_{56}La_{24}Zr_{16}O_{96}$

causes the number of lithium atoms to vary in the range from 56 to 53 and creates lithium vacancy defects in LLZO, resulting in the formation of a structure represented by a formula of $Li_{56-x}La_{24}Zr_{16}O_{96}$, where $0 \leq x \leq 4$, and x stands for the lithium atoms removed from the unit cell. However, Al or Ga doping to the Li site, however, causes substitutional defects in the LLZO and gives rise to a structure $Li_{7-3x}M_xLa_3Zr_2O_{12}$ (M = Al, Ga) ($0 \leq x \leq 0.625$). The primary findings of this thesis are as follows:

- In the case of removing more lithium atoms away from the LLZO, there is a threshold density for lithium vacancy defects in LLZO, above which the material may theoretically achieve a higher conductivity but will become thermodynamically unstable.
- Likewise, in the case of cation doping, there is a threshold for structural stability of both Al-doped and Ga-doped structures, and the compounds remain synthesizable till their fastest ionic conductivity configuration, representing the optimal dopant content to achieve synthesizable compounds.

A brief outline of this thesis is given below:

- Chapter 2 presents the methodology of atomic simulations employed in this thesis. First, the fundamentals of Density Functional Theory (DFT), including the Kohn-Sham equations, are described. Then, an overview of classical molecular dynamics (MD) is introduced. Next, energy minimization, diffusivity and conductivity calculations, structural stability calculation are also described in the methodology chapter.
- Chapter 3 discusses the relationship between lithium vacancy defects and the ionic conductivity and phase stability of LLZO material. The chapter is structured as follows: first, *ab initio* DFT simulations were performed to examine the dependence of the

diffusivity on temperatures for LLZO unit cell with the number of lithium ions ranging from 56 to 53, where 56 lithium atoms correspond to the stoichiometric LLZO. The ionic conductivity was then calculated at the temperature range of 1000 to 2500 K and the ionic conductivity of LLZO structures with different lithium concentrations in the unit cell at room temperature was extrapolated. The activation energy and the phase stability of the LLZO with different structures as a function of the number of lithium atoms were also calculated using DFT calculations.

- Chapter 4 addresses how doping the Li-site of LLZO with Al/Ga dopants affects the conductivity and stability properties of Al-doped and Ga-doped LLZO structures. We investigated the effect of changing the dopant concentration of $Li_{7-3x}M_xLa_3Zr_2O_{12}$ (M = Al, Ga) ($0 \leq x \leq 0.625$) on conductivity, activation energy, and structural stability of the doped LLZO. This chapter is structured as follows: first, *ab initio* DFT simulations were performed to study the dependence of the diffusivity on temperatures for Al-doped and Ga-doped LLZO unit cells with varying Al/Ga content present in the unit cell ranging from 1 to 5. The ionic conductivity was then calculated at the temperature range of 1000 to 2500 K, and the ionic conductivity of LLZO structures with different dopant concentrations was extrapolated for the room temperature (30°C). Finally, the activation energy and structural stability of the LLZO with different doped structures as a function of the number of dopant atoms (i.e., Al/Ga) were calculated using *ab initio* MD.
- Finally, chapter 5 concludes this thesis with a summary of our findings and possible extensions.

2. THEORETICAL BACKGROUND AND METHODS

2.1. Introduction

In the early 20th century, the quantum mechanics paradigm began as classical mechanics was unable to explain the phenomena at speeds comparable to that of lights [50]. Quantum mechanics was also found a potential new field of study for explaining the behavior of subatomic particles such as electrons. Heisenberg and Schrödinger are two pioneers in developing the formulations of quantum mechanics to describe the electronic structures of microscopic systems. Both the formulations represent the same concept from different perspectives and can work only for non-relativistic phenomena. The non-relativistic time-dependent Schrödinger equation is written as follows:

$$i\hbar\frac{\partial\phi(\boldsymbol{r},\sigma,t)}{\partial t} = \hat{H}\psi(\boldsymbol{r},\sigma,t) \tag{2.1}$$

where $\hat{H}$ is the Hamiltonian operator, $\hbar$ is the Planck constant. The wave function, $\psi(\boldsymbol{r},\sigma,t)$ describes the state of any physical system at time, t with σ as the spin coordinates and **r** as the position of all particles. For a particle of mass, m moving in a time-dependent potential V(**r**, t), the Hamiltonian operator, $\hat{H}$ is written as follows:

$$\hat{H} = \frac{\hat{\boldsymbol{P}}^2}{2m} + \hat{V}(\boldsymbol{r},t) \tag{2.2}$$

Where the first term of Eqn. 2.2 is a kinetic energy operator. The Schrödinger equation has the following form:

$$i\hbar\frac{\partial\phi(\boldsymbol{r},\sigma,t)}{\partial t} = \frac{-\hbar^2}{2m}\nabla^2\phi(\boldsymbol{r},\sigma,t) + \hat{V}(\boldsymbol{r},t)\phi(\boldsymbol{r},\sigma,t) \tag{2.3}$$

Where $\phi(\boldsymbol{r},\sigma,t)$ represents the one-particle orbital with spin, σ at position, r, and time, t.

2.2. First-principles Calculations

2.2.1. Kohn-Sham Density Functional Theory

The Schrödinger equation is written in Eqn. 2.1 is extremely complex, and a couple of assumptions are made to simplify this equation. First of them, the system is time-independent and non-relativistic. Second, the Born-Oppenheimer (BO) approximation [51] states that the nuclei are more massive than electrons, so their velocities are comparatively lower. Therefore, the nuclei seem static to the electrons and electrons can be assumed to be completely relaxed at any moment of atomic movement. Under the BO assumption, only the electronic part is considered quantum-mechanically. Third, the electrons are assumed to be in their ground state. Considering all the above mentioned assumptions, the Schrödinger equation is given by

$$\widehat{H}_{el}\psi_{el} = E_{el}\psi_{el}(\boldsymbol{r}) \tag{2.4}$$

Where E is the total energy of the system, and **r** is the coordinate of electrons.

Solving Eqn. 2.4 is still unattainable except for the smallest hydrogen systems. Density Functional Theory (DFT) formulated by Hohenberg and Kohn (HK) [52] simplifies the method by mapping a system of interacting electrons on to a system of non-interacting one-electron [53]. They proposed two theorems on which the modern-day DFT is erected. The first HK theorem states that for any system of interacting particles, the external potential, $V_{ext}(\mathbf{r})$, is uniquely determined by the ground-state charge density, $n_0(\mathbf{r})$. In other words, the external potential is a unique functional of density. The second theory states that a universal functional for the total energy, E[n(**r**)] of an electronic system can be defined in terms of the density. The exact ground-state is the global minimum value of this functional. The total energy expression can be represented in terms of density as follows:

$$E\,[\,n(\boldsymbol{r})] = F[n(\boldsymbol{r})] + \int V_{ext}(\boldsymbol{r})n(\boldsymbol{r})d\boldsymbol{r} \tag{2.5}$$

Where $F[n(\boldsymbol{r})]$ is a universal functional, and the global minimum energy, E_0 corresponds to the ground state charge density, $n_0(\boldsymbol{r})$. Eqn. 2.5 can be expressed for fictitious non-interacting electrons system using Kohn-Sham ansatz as follows [54]:

$$E\,[\,n(\boldsymbol{r})] = E_{kin}^{non}[n(\boldsymbol{r})] + \int V_{ext}(\boldsymbol{r})n(\boldsymbol{r})d\boldsymbol{r} + \; E_H\,[\,n(\boldsymbol{r})] + \; E_{XC}\,[\,n(\boldsymbol{r})] \tag{2.6}$$

Where $E_{kin}^{non}[n(\boldsymbol{r})]$ is the kinetic energy of a set of non-interacting electrons, $E_H\,[\,n(\boldsymbol{r})]$ is the classical Coulomb interaction, and $E_{XC}\,[\,n(\boldsymbol{r})]$ is the exchange-correlation energy.

The ground-state energy can be found using the Kohn-Sham (KS) equations, which is the same form as the time-dependent Schrödinger equation for non-interacting electrons system in an effective local potential as follows [53]:

$$\left[\frac{-\hbar^2}{2m}\nabla^2 + V_{ext}[n(\boldsymbol{r})] + \; V_H[n(\boldsymbol{r})] + \; V_{XC}[n(\boldsymbol{r})]\right]\psi_i(\boldsymbol{r}) = \; \varepsilon_i\psi_i(\boldsymbol{r}) \tag{2.7}$$

Where $\psi_i(\boldsymbol{r})$is the non-interacting single-particle wavefunction and

$$V_H[n(\boldsymbol{r})] = \frac{\delta E_H[n(\boldsymbol{r})]}{\partial n(\boldsymbol{r})} \tag{2.8}$$

And

$$V_{XC}[n(\boldsymbol{r})] = \frac{\delta E_{XC}[n(\boldsymbol{r})]}{\partial n(\boldsymbol{r})} \tag{2.9}$$

2.3. Classical Molecular Dynamics Simulations

2.3.1. Principles of Molecular Dynamics

It is generally important to study realistic modeling of systems under finite temperatures and/or pressure. For this purpose, a method of simulation can be employed that determines the time evolution of a system. This method is usually referred to as molecular dynamics (MD) simulations [55], [56]. The purpose of the MD simulations is to track the atomic interactions in terms of time using numerically solvable classical equations of motions. Newton's equation of motion is as follows:

$$\boldsymbol{F} = m\boldsymbol{a} = m\frac{\mathrm{d}v}{\mathrm{d}t} = m\frac{\mathrm{d}^2\boldsymbol{r}}{\mathrm{d}t^2} \tag{2.10}$$

The force acting on each atom can be evaluated from potential, U through

$$\boldsymbol{F} = -\nabla U(\boldsymbol{r}) \tag{2.11}$$

The structural evolution of the system can be obtained by calculating the forces on atoms as follows:

$$\boldsymbol{F_I} = -\nabla_I U(R_1, R_2, R_3, \ldots, R_N) \tag{2.12}$$

Where $U(R_1, R_2, R_3, \ldots, R_N)$ is the potential energy function of the system, and $\mathbf{R_I}$ is the instantaneous position of atom, **I**. The initial position, velocity, and net force on atoms are used to achieve the motion over time. The correct potential, *U* can be estimated in two main ways. In classical MD simulations, *U* is estimated applying parametric interatomic potentials. On the contrary, an electronic structure method, such as DFT is employed to compute the potential energy function, *U* and the forces, $\boldsymbol{F_I}$ [57]. This approach is called *ab initio* MD simulations.

2.3.2. Integrating the Equations of Motion

In practice, instead of solving a huge set of coupled differential equations, it is wise to numerically integrate the equations of motion for the atoms over a small time step (typically, a fraction of a femtosecond) to obtain the force information.

2.3.2.1. The Verlet Algorithm

The Verlet algorithm [58] is one of the most popular methods and widely used for integrating the equations of motions. According to the algorithm, the atomic positions and forces at time, t together with the position at (t - Δt) is employed to estimate the position of the particle, *I* at the next step, (t + Δt) as:

$$\boldsymbol{R_I}(\mathrm{t} + \Delta\mathrm{t}) \approx \boldsymbol{R_I}(t) + (\Delta t)\boldsymbol{V_I}(t) + \frac{(\Delta t)^2}{2M_I}\boldsymbol{F_I}(t) \tag{2.13}$$

Where $\boldsymbol{V_I}$ and M_I represent the velocity and mass of the particle *I*, respectively. By performing a similar expansion for the particle, *I* at time (t - Δt) and adding to Eqn 2.12 the following expression for the particle position is obtained:

$$\boldsymbol{R_I}(\mathrm{t} + \Delta\mathrm{t}) \approx 2\boldsymbol{R_I}(t) - \boldsymbol{R_I}(\mathrm{t} - \Delta\mathrm{t}) + \frac{(\Delta t)^2}{M_I}\boldsymbol{F_I}(t) \tag{2.14}$$

Eqn. 2.13 is known as the Verlet integrator to obtain the trajectory of a particle of time step Δt.

2.3.2.2. The Velocity Verlet Algorithm

The verlet algorithm does not propagate the complete phase space trajectory. Another disadvantage is that this algorithm requires memory at both times t and $\mathrm{t} + \Delta\mathrm{t}$. The velocity verlet algorithm deals with the time-reversibility of Newton's equations of motion and is employed to overcome the mentioned shortcomings. Thus, if the starting time in Eqn. 2.12 is $\mathrm{t} + \Delta\mathrm{t}$ and the time-step of the motion is $-\Delta\mathrm{t}$, the equation can be written as:

$$\mathbf{v}\boldsymbol{R_I}(\mathrm{t}) \approx \boldsymbol{R_I}(t + \Delta\mathrm{t}) + (-\Delta t)\boldsymbol{V_I}(t + \Delta\mathrm{t}) + \frac{(\Delta t)^2}{2M_I}\boldsymbol{F_I}(t + \Delta\mathrm{t}) \tag{2.15}$$

By substituting the value of $\boldsymbol{R_I}(t + \Delta\mathrm{t})$ from Eqn. 2.12 to Eqn. 2.14, it can be written that

$$\boldsymbol{V_I}(t + \Delta\mathrm{t}) \approx \boldsymbol{V_I}(t) + \frac{\Delta t}{2M_I}[\boldsymbol{F_I}(t) + \boldsymbol{F_I}(t + \Delta t)] \tag{2.16}$$

Eqn. 2.12 and 2.15 are known as the velocity Verlet algorithm [59]. This algorithm provides both the position and velocity of atoms simultaneously and resolves the drawbacks of verlet algorithm explained earlier. The time-reversal symmetry is a fundamental property of classical equations of motion, and it is indeed preserved by both the Verlet and velocity Verlet algorithms.

2.3.3. Statistical Ensembles

In real experiments, there are some experimental parameters such as volume, pressure, and temperature, which are controlled during the synthesis or characterization. Different statistical

ensembles have been introduced to integrate these actual experimental conditions to computational modeling. A short description of these ensembles is given below:

2.3.3.1. NVT Ensemble

This is a constant volume and constant temperature ensemble, which is also known as the canonical ensemble. This might be the best way to equilibrate system pressure initially. In other words, the NVT ensemble allows one to fix the system pressure for the material at any phase while equilibrating the initial structure. To perform conformational exploration of molecules, NVT without boundary conditions is widely used. This approach is often useful while working with chemical reaction in gaseous material as system pressure is irrelevant.

2.3.3.2. NPT Ensemble

This is a constant pressure and constant temperature ensemble that allows the system to change the volume and flow in or out the energy at constant pressure and temperature. In every step, the unit cell vectors are adjusted to obtain the targeted pressure. This can be the best option to fix the system equilibration volume and densities at a predetermined pressure. It is a good practice to perform initial geometrical relaxation of any material or interatomic potential using NPT or NVT ensembles before performing any kind of simulation.

2.3.3.3. NST Ensemble

This is constant stress and constant temperature ensemble, which can be considered as a specific type of NPT ensemble that allows the user to tune the stress tensor for xx, yy, zz, xy, yz, and zx components. This ensemble is used for analyzing the stress-strain correlation of materials.

2.3.3.4. NPH Ensemble

Enthalpy, H is the sum of the internal energy of the system and the product of its volume and pressure. NPH is a constant pressure and constant enthalpy ensemble, which is equivalent to

the NVE ensemble, but NPH allows to control the system pressure without controlling the system volume.

2.3.4. *Ab initio* Molecular Dynamics

Ab initio molecular dynamics (AIMD) simulations are used to obtain the force fields using the expectation value of the total energy in the electronic ground state as follows:

$$F_I = -\nabla_I \langle \psi_0 | \hat{H} | \psi_0 \rangle \tag{2.17}$$

Where $\hat{H}$ is the total Hamiltonian of the system, ψ_0 denotes the ground-state wavefunction with energy $E_0(\{\boldsymbol{R_I}\})$, that is

$$\hat{H}|\psi_0\rangle = E_0|\psi_0\rangle \tag{2.18}$$

Here, $\boldsymbol{R_I}$ represents the atomic positions. The electronic ground state is characterized by atomic positions. At each AIMD step, the new electronic ground state is solved to calculate the forces according to Eqn 2.16. The electronic charge distribution associated with the ground state acts as an external field working for the nuclei. Afterward, the nuclei, which are treated classically, are propagated in time with algorithms introduced above. Calculation of the derivatives in Eqn. 2.16 is performed using the Hellmann-Feynman theorem as follows:

$$\begin{aligned} F_I = -\nabla_I \langle \psi_0 | \hat{H} | \psi_0 \rangle &= -E_0 \langle \nabla_I \psi_0 | \psi_0 \rangle - \langle \psi_0 | \nabla_I \psi_0 \rangle E_0 - \langle \psi_0 | \nabla_I \hat{H} | \psi_0 \rangle \\ &= -E_0 \nabla_I \langle \psi_0 | \psi_0 \rangle - \langle \psi_0 | \nabla_I \hat{H} | \psi_0 \rangle \end{aligned} \tag{2.19}$$

Considering the orthonormality condition, $\langle \psi_0 | \psi_0 \rangle = 1$,

$$F_I = -\langle \psi_0 | \nabla_I \hat{H} | \psi_0 \rangle \tag{2.20}$$

However, Eqn. 2.19 is not valid for the atomic-orbital basis functions, and extra terms are added on the right side of the equation. These additional terms are generally referred to as Pulay forces. The Pulay forces vanish if the basis set is complete [60].

The thesis is dedicated to the investigation of Li-ion diffusion in lithium deficient and doped LLZO structures using AIMD simulations. These calculations are performed in the canonical ensemble (NVT) while the temperature of the system is controlled by the Nosè-Hoover thermostat.

2.4. Computational Details

2.4.1. Implementation

The overall work presented in this thesis can be divided into a couple of segments, as shown in figure 1. Python scripts were developed to generate atomic structures that were then used as input structures for DFT calculations. The overall jobs performed in python can also be classified into a couple of steps, as mentioned in figure 2. All the input scripts are available in the Appendix. All density functional theory calculations in this study were performed using the Vienna *Ab initio* Simulation Package (VASP) [61]. The Projector augmented-wave (PAW) approach was used to treat the interaction between valence electron and ion [62]. All the total energy calculations were performed using the Perdew-Burke-Ernzerhof (PBE) generalized gradient approximation (GGA) [63]. We used the Monkhorst-Pack scheme to create the K-space matrix. The INCAR scripts for all VASP calculations have been added to the Appendix. Then, nMoldyn software has been used for trajectory analysis. MATLAB has been used for the curve fitting and diffusivity calculations to obtain the diffusivity-temperature relationship.

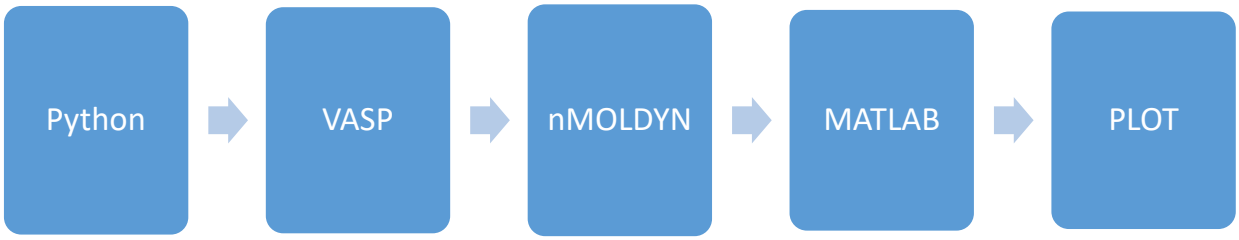

Figure 2.1. Overview of the steps of calculation

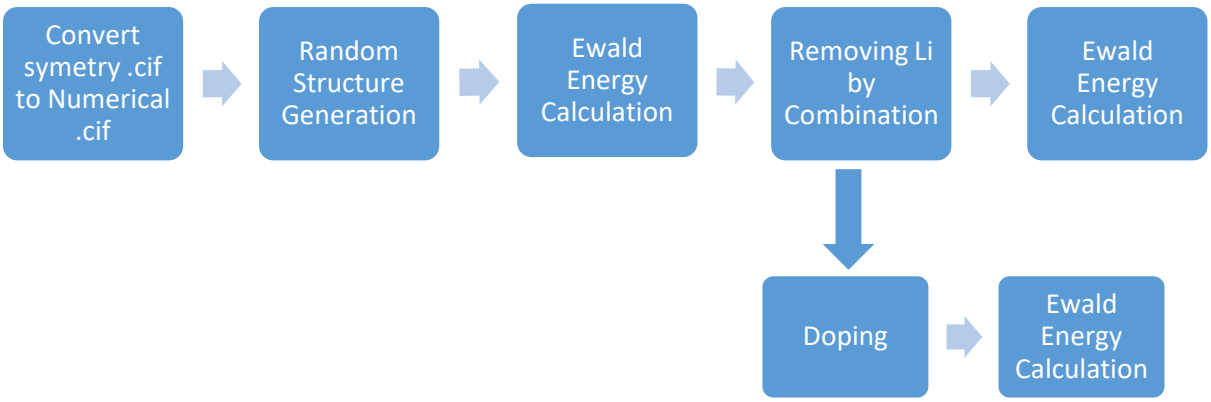

Figure 2.2. Steps of jobs performed with Python

2.4.2. Initial Structure Optimization

The calculation of cubic structure garnet LLZO is based on a unit cell ($Li_{56}La_{24}Zr_{16}O_{96}$) containing eight formula units ($Li_7La_3Zr_2O_{12}$). The unit cell has a structure with La and Zr ions located in the centers of LaO_8 dodecahedrons and ZrO_6 octahedrons, respectively, O ions fully occupying the 96h sites in the structure, and lithium ions partially occupying 24d tetrahedral and 96h octahedral sites [12], [37], [45], as shown in figure 1.4. The initial disordered structure was obtained from the ICSD (CC: 422259). The crystallographic information file contains the cubic structure with cell dimensions of a = b = c = 12.9827 Å and volume 2188.2407 $Å^3$. It is worth

noting that the obtained cubic structure is disordered and contains excess Li sites because of the partial occupation of lithium atoms in 24d and 96h sites (Fig. 1). The number of available lithium sites is considerably larger than the number of lithium ions. To prepare the initial structures of the LLZO unit cell with 56 Li-ions, lithium ions were first arranged based on the site occupancy factors with electrostatic energy criterion [64] implemented in the Python Materials Genomics (pymatgen) analysis code [65]. Prior to removing lithium atoms from the disordered structure, the ions were assigned with idealized oxidation states, i.e., Li^{1+}, La^{3+}, Zr^{4+}, O^{2-}. Given a large number of possible permutations of Li positions ($>10^{11}$), a random sampling approach for generating random structures was used. The number of lithium atoms in those randomly generated geometries was kept constant at 56 as per the stoichiometric structure requirement. Li atoms were removed using a simple strategy that involves the site occupancies published by Awaka et al. [66]. For the initial structure generation, a total of 20,000 random structures were generated. The structures were ascendingly sorted based on Ewald summation[64], and those which reach the lowest Ewald energies were chosen. Since finding the exact ground state lithium arrangement was not a necessity for the diffusion properties, the approach of having structures up to the desired Ewald energy was chosen instead of finding the structure with lowest electrostatic energy configuration.

2.4.3. *Ab initio* Molecular Dynamics Conductivity Calculations

For the diffusivity and conductivity calculations, *ab initio* molecular dynamics (AIMD) simulations based on the Born-Oppenheimer approximation were performed using VASP. The AIMD calculations were obtained for the simulation time up to 25 ps with the time step of 1 fs. The relaxed ground-state structures were used as the initial structures and were heated from an initial temperature of 10 K to the desired temperatures of 1000 to 2500 K at a constant rate. The MD simulations were performed in the canonical ensemble with a constant number of particles,

volumes, and temperature (NVT) using a Nose-Hoover thermostat. nMoldyn (version 4.0.0) [67] was used for the post-processing of the AIMD calculations.

The diffusion properties were calculated using the trajectory analysis of the lithium ions, $r_i(t)$, obtained from AIMD simulations. The displacement, Δr_i of ion, i from time, t_1 to t_2 can be calculated as:

$$\Delta r_i(\Delta t) = r_i(t_2) - r_i(t_1) \tag{2.21}$$

Where $\Delta t = t_2 - t_1$ is the time interval. The total squared displacement for N mobile ions over Δt time interval is calculated as $\sum_{i=1}^{N}(|\Delta r_i(\Delta t)|^2)$. This describes the movement of all N mobile ions over a time interval, Δt. The mean square displacement (MSD) for all diffusional ions is calculated as:

$$\text{TMSD}(\Delta t) = \sum_{i=1}^{N}\langle|r_i(\Delta t) - r_i(0)|^2\rangle \tag{2.22}$$

The mean square displacement (MSD) is calculated as the TMSD per mobile ion as [68]:

$$\text{MSD}(\Delta t) = \frac{1}{N}\text{TMSD}(\Delta t) \tag{2.23}$$

By averaging over The self-diffusion coefficient, D of Li-ions was determined according to the Einstein relation as follows:

$$D = \frac{\text{MSD}(\Delta t)}{2d(\Delta t)} \tag{2.24}$$

Where d = 3 is the dimension of the lattice where the diffusion takes place, and $\langle[r(\Delta t)]^2\rangle$ is the square displacement (SD) of Li ions. The calculated diffusion coefficient fluctuates due to the statistical uncertainty in the linear fitting. From the diffusivity D, ionic conductivity was calculated according to the Nernst-Einstein relationship [68], [69]:

$$\sigma = \frac{Nq^2}{Vk_BT}D \tag{2.25}$$

Where V is the total volume of the model system, q is the charge of the mobile-ion species, T temperature, and k_B Boltzmann constant. Therefore, the lithium-ion conductivity of LLZO is determined by the concentration of the mobile lithium ions, which can be tuned by doping. Combining Eqn 2.24 and 2.25, the dependence of total ionic conductivity can be expressed in terms of Arrhenius type behavior, as follows:

$$\sigma T = \text{A} \exp(\frac{-E_a}{k_B T}) \tag{2.26}$$

Where A is a prefactor, T is the absolute temperature, and E_a denotes the corresponding activation energy.

2.4.4. Phase Stability

The phase stability of predicted materials has been estimated by constructing the convex energy hull of all relevant phases in the compositional phase diagram. The phase equilibria at the composition C corresponding to the energy minimum $E_{eq}(C)$ were identified by comparing the energy of all relevant phases in its compositional space. The phase stability of the investigated phase was evaluated using the decomposition energy, ΔE_{de} (phase) = $E_{eq}(C)$ – E (phase), of a given phase to its phase equilibria. ΔE_{de} is the negative of energy above hull. In general, a stable compound should have a energy above hull, ΔE of 0 [70] at 0 K. A positive value of the energy above hull, ΔE suggests that the corresponding phase is not thermodynamically stable. The higher the ΔE is, the more unstable the compound is [70], [71].

3. LITHIUM IONIC CONDUCTIVITY AND STABILITY OF CUBIC $Li_7La_3Zr_2O_{12}$ SOLID ELECTROLYTE WITH Li-VACANCY DEFECTS

3.1. Introduction

The cubic LLZO is much more conductive with a high degree of the disorder [36]. The reported conductivity of cubic LLZO structure at room temperature [37] is on the order of ~10^{-4} S/cm, which is about two orders of magnitude higher than that of the tetragonal structure (~10^{-6} S/cm) [34], [38]. The cubic LLZO has therefore drawn a lot of attention and has been extensively studied in anticipation of being used for solid lithium batteries. Mathematical modeling of solid electrolytes [72], [73] is an undeniable way to gain atomic-level insight into Li-ion diffusion and conduction towards lowering the activation energy and increasing high ionic conductivity. However, a detailed study of the impacts of Li-ion defects on the ionic conductivity and phase stability still lacks in the literature. Li defects in the LLZO material mainly include vacancies, interstitials, and Frankel-type vacancy-interstitial pair defects [48]. From the defect engineering perspective, removing lithium atoms from the stoichiometric LLZO is the most straightforward way to create lithium vacancy defects. This study aims to investigate the relationship between lithium vacancy defects and the ionic conductivity and phase stability of LLZO material using first-principles-based computation, in anticipation of suggesting ways to increase the conductivity of the LLZO material.

3.2. Method of Calculation

The geometrical optimization of the initial cubic LLZO structure has already been described in section 2.4.2. The python code for ‘random structure generation’ has been added to

the appendix. To determine the ground-state structure of cubic LLZO with certain lithium atoms removed, the Pymatgen package was used to generate a total of $^{56}C_{55,}$ $^{56}C_{54,}$ or $^{56}C_{53}$ distinctive structures corresponding to removing 1, 2, or 3 lithium atoms from the stoichiometric LLZO structure, respectively. The python code for 'removing lithium following combination' has been added to the appendix. All structures were selected according to the lowest electrostatic energy and DFT energy to obtain the ground-state structures of cubic LLZO with 55, 54, or 53 lithium atoms in a unit for the AIMD simulations. The python code for 'Ewald energy calculation' has also been added to the appendix. All structures were relaxed through the DFT calculations to obtain a structure with the ground-state structure having the lowest DFT energy for *ab initio* molecular dynamics (AIMD) simulations.

3.3. Results and Discussion

3.3.1. The Diffusivity of Lithium Ions

Figure 3.1 shows the Arrhenius plot for the diffusion coefficient, D of lithium ions in the cubic stoichiometric LLZO, i.e., $Li_7La_3Zr_2O_{12}$. It reveals that the diffusivity increases from 1.31×10^{-5} cm^2/s to 4.78×10^{-5} cm^2/s as the temperature increases from 1000 K to 2200 K.

Similar AIMD simulations were performed to calculate the lithium-ion diffusivity of LLZO with 55, 54, and 53 lithium atoms. As shown in figure 3.1, in the temperature range from 1000 K to 2500 K, the diffusivities of LLZO with 56, 55, 54, and 53 lithium atoms all change following an Arrhenius-type relationship [74]. The LLZO with the stoichiometric composition (i.e., 56 lithium atoms) shows the lowest Li-ion diffusivity among all the structures investigated in the present work. This is due to the fact that all lithium sites are filled, or in other words, and the lithium vacancy density is zero. The removal of lithium atoms from the stoichiometric structure results in the formation of lithium vacancy defects, accordingly leading to an increase in the

diffusivity. The removal of lithium atoms from the stoichiometric structure decreases the binding energy of the neighboring Li-ions and consequently makes the crystal structure distorted. This allows the remaining lithium atoms to diffuse at a higher rate [44].

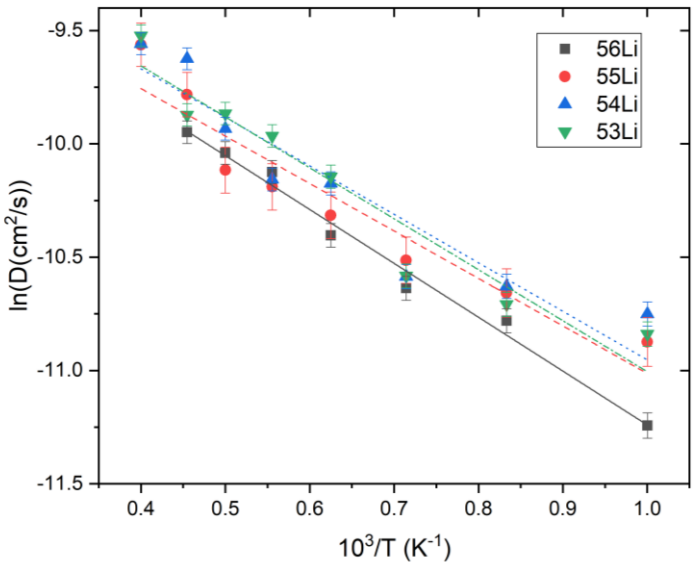

Figure 3.1. Logarithm of the diffusion coefficient for different number of lithium ions in the crystalline cubic LLZO unit cell. The solid straight line (black) indicates the linear fit of the points for stoichiometric LLZO structure. The dashed lines, red, blue, and green, represents the linear fit of the points for cubic LLZO structure with 55, 54, and 53 lithium ions, respectively. The error bars stand for the statistical uncertainty in the linear fitting.

3.3.2. The Conductivity of Lithium Ions

The conductivity was calculated based on the diffusivity with Eqn. 2.25. The conductivities at room temperature and the values of activation energy are shown in figure 3.2. It was revealed that the conductivity of stoichiometric cubic LLZO at room temperature is 2.72×10^{-3} S/cm. With reducing the number of lithium atoms in the unit cell to 55, 54, and 53, the conductivity increases to 1.43×10^{-2}, 3.67×10^{-2}, and 5.00×10^{-2} Scm^{-1}, respectively. The calculated conductivities were compared with the reported computational and experimental results to confirm the validity of the obtained simulation results. For stoichiometric cubic LLZO, the extrapolated conductivity at room temperature (2.72×10^{-3} S/cm), and calculated activation energy (0.25eV) are in agreement with

reported conductivity at 300 K and activation energy for AIMD simulations [75], [76]. These results of 55 lithium atoms are also in agreement with the conductivity 2.92×10^{-2} S/cm (at 300 K) for cubic $Li_{6.875}La_3Zr_2O_{12}$ (corresponding to 55 lithium atoms) in the literature reported by Jian et al. [76].

3.3.3. Activation Energy

The values of activation energy were calculated through the absolute value of the slopes of the ln(D)-10^3/T curves shown in figure 3.2 using Eqn 2.24. The activation energy, E_a in stoichiometric cubic LLZO, was found to be 0.25 eV. This is basically in agreement with the values reported in the literature, 0.19-0.28 eV [12], [76], [77]. The reported activation energy of lithium-ions in LLZO is lower than the typical experimental values of activation energies reported (0.32-0.41) [78]–[80]. Such activation energy is lower than the computational activation energy of tetragonal LLZO, which is typically in the range of 0.4-0.6 eV [34], [44], [80]–[82]. The activation energy out of our calculation is also comparable to the experimental values of 0.25 to 0.36 eV [78], [79], [83]. There are three factors working together for this improvement of activation energy in MD simulation compared to the experimental reported values [4]. Firstly, it is tough to separate the contribution of bulk conductivity from the grain boundary resistance using impedance spectroscope. For this reason, most of the experiments neglect the contribution of bulk conductivity. Secondly, simulations were are performed at high temperatures (≥1000 K), where the garnet can turn into disordered phase and the change of lithium ion activation energy will be larger than the corresponding room temperature values. This is also supported by classical MD results [48]. Thirdly, the cubic garnet structures built for the calculation were disordered with high conductivity, while at room temperature the structures tend to adopt an ordered tetragonal phase in the experiments. The lowest activation energy, $E_a = (0.16 \pm 0.008)$ eV is obtained for LLZO

with the lowest lithium concentration, i.e., consisting of 53 Li atoms in the unit cell. The low activation energy originates from the formation of a large amount of lithium vacancy defects in the case of non-stoichiometric LLZO. The lithium-ion vacancy defects increase the local electric field from the nearest negative oxygen ions, which causes a decrease in the Li-ion migration barriers [44]. Our work reveals that, when increasing the number of lithium atoms removed from the stoichiomitric LLZO , there are an approximate linear increase in the conductivity and an approximate expotential decay of the activation energy, as shown in figure 3.2. This is reasonable while considering the exponential relatioship between the conductivity and activation energy as reflected in Eq. (4).

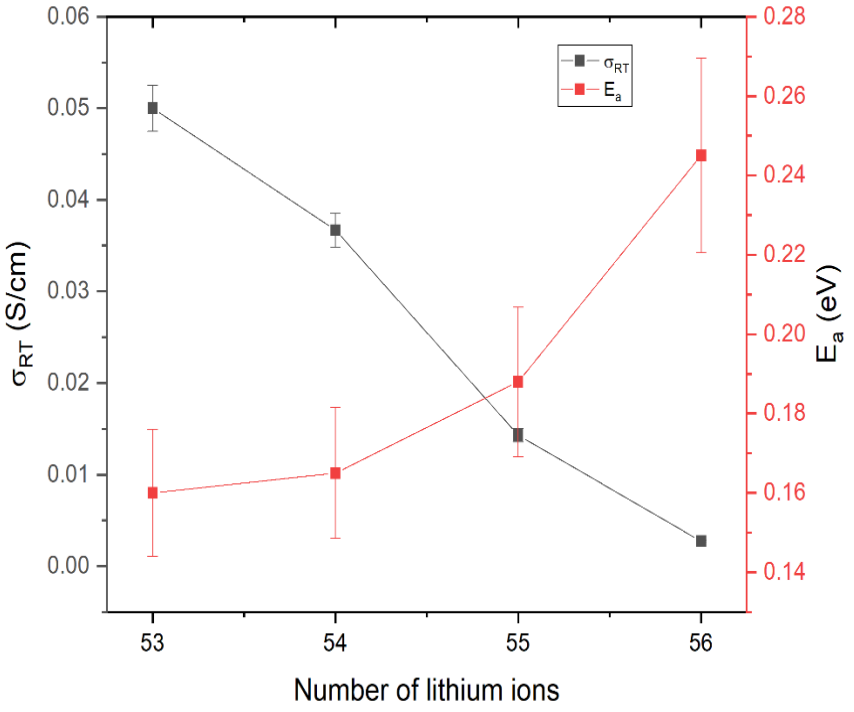

Figure 3.2. Dependency of the room temperature conductivity, σ_{RT} and the activation energy, E_a of the number of lithium ions in the LLZO unit cell (derived from figure 3.1).

3.3.4. Phase Stability

Phase stability of cubic LLZO with the number of lithium atoms varying from 53 to 56 atoms in a unit cell was studied by means of energy above hull, ΔE. Firstly, the DFT energies and Ewald energies were calculated for all generated structures of LLZO with 56, 55, 54, and 53 lithium atoms in the unit cell. Then the generated structures were sorted based on the calculated energies, and a set of ten structures up to the desired DFT and Ewald energies were chosen. These selected structures with the lowest DFT and Ewald energies were then used for the calculation of energy above hull, ΔE using the pymatgen toolkit [65]. The average of the calculated ΔE for ten structures gives an overview of the thermodynamic stability of the materials at 0 K, as shown in Table 2. It can be seen that All cubic LLZO structures with different number of lithium atoms in the unit cells are slightly metastable at 0 K with small ΔE (≤30 meV/atom) [70]. Considering the volume of a unit cell of the cubic LLZO (V = 2188.24 $Å^3$), the density of vacancy defects (i.e., the fraction of the number of removed Li atoms to the number of total atoms in a unit cell) of the LLZO with different concentrations of lithium vacancies was calculated. A clear trend of phase stability as a function of the density of Li vacancy defects in the crystal unit cell is observed (table 1). The stoichiometric LLZO presents the lowest energy above hull, 11.629 meV/atom, indicating the best stability. Such a value of the energy above hull is basically in agreement with that of 7 meV/atom reported by Yizhou et al. [84]. Based on our calculations, removing one lithium atom from the unit cell increases the value of energy above hull from 11.629 to 15.167 meV/atom, and removing two or three will lead to the values of 19.575 and 24.123 meV/atom, respectively.

It is generally considered that compounds with ΔE below 25 meV/atom can be stabilized with entropic effects [75]. Thus, considering the energy above hull we calculated, it is likely to suggest that increasing the lithium ionic conductivity of cubic LLZO solid electrolyte by removing

lithium atoms to introduce lithium vacancy defects is only feasible when three lithium atom is removed from a unit of $Li_{56}La_{24}Zr_{16}O_{96}$. It corresponds to LLZO with a composition of $Li_{6.625}La_3Zr_2O_{12}$. In other words, when more than three lithium atoms are removed from the LLZO unit cell, the material will gain energy above hull more than 25 eV and become thermodynamically unstable enough to be synthesized in the experiment.

Table 3.1. Energy above hull, ΔE of the cubic LLZO obtained for different densities of Li vacancy defects in the crystal unit cell. The density of the vacancy defect is the ratio of the number of lithium removed from the unit cell and the volume of the unit cell.

Composition	Number of Li atoms	Density of Li Vacancy Defects (Å^3)	Energy Above Hull, ΔE (meV/atom)
$Li_7La_3Zr_2O_{12}$	56	0	11.629
$Li_{6.875}La_3Zr_2O_{12}$	55	4.57×10^{-4}	15.167
$Li_{6.75}La_3Zr_2O_{12}$	54	9.14×10^{-4}	19.575
$Li_{6.625}La_3Zr_2O_{12}$	53	1.37×10^{-3}	24.123

3.4. Conclusion

In summary, the first-principles calculations were performed using the *ab initio* density functional theory to study the Li ion diffusivity, room temperature conductivity, and phase stability of the garnet-type cubic LLZO material with varying lithium-ion concentration, ranging from 53 to 56 atoms (56 lithium atoms represent the stoichiometric concentration). The computational results reported in this chapter confirms that the Li-ion self-diffusion has an observable dependency on the number of lithium atoms in the LLZO unit cell. The activation energy for the stoichiometric LLZO structure has been calculated as 0.25 eV. The activation energy of lithium-ion diffusion gradually decreases from 0.25 eV to 0.16 eV with the removal of lithium atom from the stoichiometric LLZO unit cell. This indicates that the increase in lithium vacancy concentration in LLZO leads to a decrease in activation energy. The Arrhenius-type plots of the ionic conductivities of cubic LLZO for the different number of lithium atoms as a function of

temperature has been used for the extrapolation of conductivity at room temperature (30°C). The room temperature conductivity versus lithium vacancy concentration shows that the maximum room temperature conductivity and minimum activation energy can be seen for cubic LLZO structure with 53 lithium atoms in the unit cell. σ_{RT}=50 mS/cm and E_a=0.16 eV represents the room temperature conductivity and activation energy, respectively for the cubic LLZO structure containing 53 Li atoms in the crystal unit cell. Furthermore, the phase stability of the cubic LLZO structures containing the different number of lithium atoms in the unit cell has also been calculated in terms of energy above hull at 0 K. The computational results reported in this chapter demonstrate that with the removal of lithium atom from the LLZO unit cell, the structures gradually become more prone to decomposition. This indicates that the stoichiometric cubic LLZO structure is the most stable structure with energy above hull, ΔE = 11.63 meV/atom. The simulations suggest that there is an inverse relationship between the phase stability and the room temperature conductivity of the cubic LLZO structures with different number of lithium ions in the unit cell, ranging from 53 to 56. A reduction of the lithium atom number from the stoichiometric content (56 Li atoms) leads to an increase in room temperature (30°C) conductivity and the decrease of thermodynamic stability. It appears that the knowledge obtained through the establishment of the AIMD simulation procedure for the quantification of diffusion coefficient, room temperature conductivity, and phase stability will help design fast lithium ionic conductors in the future.

4. EFFECT OF DOPING ON THE IONIC CONDUCTIVITY AND STABILITY ON THE GARNET $Li_{7-3x}M_xLa_3Zr_2O_{12}$ (M = Al, Ga) ($0 \leq x \leq 0.625$)

4.1. Introduction

The cubic structure of LLZO exhibits a disordered lithium-ion distribution and lithium vacancy that results in the instability of cubic LLZO at room temperature. In order to achieve a more conductive cubic structure, it is highly required to stabilize the cubic structure [85]–[93]. The cubic garnet type LLZO has therefore drawn a lot of attention and has been extensively studied in anticipation of being used for solid lithium batteries. However, these cubic LLZO crystal structures can be stabilized by supervalent substitution at the Li, La, or Zr crystallographic sites. Most doping strategies have been adopted to stabilize the crystal structure with high conductivity at room temperature without obstructing other useful properties. Al^{3+} and Ga^{3+} that substitute on the Li^+ site [3], [17], [20]–[24], as well as Ta^{5+}, Nb^{5+}, Te^{6+}, and W^{6+} that substitute in the Zr sublattice, have been employed to stabilize the cubic LLZO [99]–[102]. Intentional substitution of both the Li^+ and Zr^{4+} sites has been proven successful. Due to high charge difference between the hosting cation, Li^+ and the dopants (Al/Ga), doping the Li^+ site with substituent (i.e., Al/Ga) results in a rapid decrease in lithium content, leading to the composition $Li_{7-3x}M_xLa_3Zr_2O_{12}$ (M = Al, Ga). Two Li site vacancies are created for every addition of Al^{3+} or Ga^{3+}. In common with Al-doped cubic LLZO, the Ga-doped cubic LLZO has demonstrated promising structural and transport properties. However, researchers have already reported how the incorporation of foreign ions (i.e., Al/Ga) in the Li sublattice affects the structure, topology (i.e., migration pathway), Li^+ ion dynamics, and conductivity of doped structures. Until now, the density functional theory (DFT)

calculations for the optimal Al/Ga dopant concentration that maximizes conductivity of Al/Ga doped cubic LLZO and the analysis of structural stability are still lacking in the literature.

This study aims to investigate the dependence of the ionic conductivity and structural stability on the dopant concentration of cubic LLZO material using first-principles-based computation, in anticipation of suggesting the optimal dopant concentration to obtain the maximum conductivity of the LLZO material. We investigated the effect of changing the dopant concentration of $Li_{7-3x}M_xLa_3Zr_2O_{12}$ (M = Al, Ga) ($0 \leq x \leq 0.625$) on conductivity, activation energy, and structural stability of the doped LLZO. Our research work is structured as follows: first, *ab initio* DFT simulations were performed to study the dependence of the diffusivity on temperatures for Al-doped and Ga-doped LLZO unit cells with varying Al/Ga content present in the unit cell ranging from 1 to 5. The ionic conductivity was then calculated at the temperature range of 1000 to 2500 K, and the ionic conductivity of LLZO structures with different dopant concentrations was extrapolated for the room temperature (30°C). The activation energy of the LLZO with different doped structures as a function of the number of dopant atoms (i.e., Al/Ga) was also calculated. Our density functional theory (DFT) calculations reveal that there is a threshold for the density of dopant atoms in LLZO, above which the material conductivities start to decrease. After the structural stability analysis, it was also concluded that there is a threshold for structural stability of both Al-doped and Ga-doped structures, and the compounds remain synthesizable till their fastest ionic conductivity configuration, representing the optimal dopant content to achieve synthesizable compounds.

4.2. Method of Calculation

The geometrical optimization of the initial cubic LLZO structure has already been described in section 2.4.2. For doped compositions, a similar approach was adopted. In addition to

ordering the lithium atoms, the dopants were also ordered. The amount of dopant (i.e., Al/Ga) has been varied incrementally from 1 to 5 in the cubic LLZO unit cell. For each of the configurations, both lithium atoms and dopants are ordered using Pymatgen. As Al/Ga is known to substitute to Li, the occupancy of the supervalent Al^{3+} or Ga^{3+} in the Li^{+} induced two lithium vacancies near the dopant atom(s) to balance the charge neutrality [38]. Accordingly, the doping lithium site resulted in Li vacancy from the stoichiometric cubic LLZO structure obtained above, leading to the composition $Li_{7-3x}M_xLa_3Zr_2O_{12}$ (M = Al, Ga) where x varies from 0 to 0.625. All the structures were sorted in terms of lowest electrostatic energy and DFT energy to obtain the ground-state structures of cubic LLZO with varying dopant (i.e., Al/Ga) concentration, ranging from 1 to 5 atoms per unit cell, for the AIMD simulations. The python code for 'doped structure generation' has been added to the appendix.

All structures were relaxed through the DFT calculations to obtain a structure with the ground-state structure having the lowest DFT energy for *ab initio* molecular dynamics (AIMD) simulations.

4.3. Result and Discussion

4.3.1. Lithium Diffusivity, Conductivity, and Activation Energy

The synthesis of this material was found to be difficult and it was finally shown that aluminum doping is necessary to obtain dense sintered cubic LLZO polymorph with high ionic conductivity [46], [87], [89], [103]. like Al, Ga has a only one oxidation state and same charge, it also has a slightly larger size than Al (for both octahedral and tetrahedral coordination) thus, this may lead to a more open lattice and hence, higher ionic mobility and conductivity [97]. AIMD simulations were performed on Al-doped, and Ga-doped LLZO, and the effect of Al^{3+} and Ga^{3+} doping on the conductivity is shown as an Arrhenius plot in Table 2 and 3, respectively. The

extrapolated conductivity at room temperature (30°C) and activation energy calculated from DFT are summarized in figure 4(c), and 4(d). It was revealed that the conductivity of undoped cubic LLZO at room temperature is 2.72×10^{-3} S/cm, and the activation energy is 0.25 eV. As researchers have reported success in conductivity improvement by aliovalent doping on the Li-site, cubic LLZO has been doped with Al and Ga separately in our study to increase the conductivity. We investigated the effect of changing the dopant concentration of $Li_{7-3x}M_xLa_3Zr_2O_{12}$ (M = Al, Ga) ($0 \leq x \leq 0.625$) on conductivity and activation energy of the doped LLZO. Figure 4(a) and 4(b) depicts the temperature dependence of the ionic conductivity of Al-doped and Ga-doped LLZO garnets with different contents of Al and Ga dopants between 1000 K and 2500 K. The conductivity follows an Arrhenius-type temperature dependence for all the examined Al/Ga contents. With increasing the number of dopant atoms (i.e., Al/Ga) in the LLZO unit cell, the room temperature conductivity, σ_{RT} increases up to a certain dopant concentration, as shown in figure 4(c) and 4(d). For Al-doped LLZO, the fastest ionic conductivity at room temperature, σ_{RT} = 12 mS/cm observed for $Li_{5.5}Ga_{0.5}La_3Zr_2O_{12}$ is combined with the lowest activation energy, 0.18 eV, representing the optimal Al content to achieve faster ion transport in these Al-doped garnets. A Further increase in Al content in the LLZO unit cell demotes the calculated room temperature conductivity to 5.64 mS/cm. Similarly, σ_{RT} rises with the increase of Ga-dopant content in the LLZO unit cell and reaches a maximum of 16.8 mS/cm leading to $Li_{5.875}Ga_{0.375}La_3Zr_2O_{12}$. A further increase in Ga content leads to a decrease in ionic conductivity along with an increase in activation energy. The obtained total ionic conductivity and activation energy for $Li_{6.25}Ga_{0.25}La_3Zr_2O_{12}$ is 3.28 mS/cm and 0.22 eV, respectively. These results are generally in agreement with the 1.46 mS/cm total conductivity and 0.25 eV activation energy reported in the literature for $Li_{6.25}Ga_{0.25}La_3Zr_2O_{12}$ [104].

Table 4.1. Temperature dependence of the conductivity obtained with AIMD simulation for Al-doped LLZO structures ($Li_{7-3x}Al_xLa_3Zr_2O_{12}$)

Temperature, T (K)	log(σT) [S/cm] (x = 1)	log(σT) [S/cm] (x = 2)	log(σT) [S/cm] (x = 3)	log(σT) [S/cm] (x = 4)	log(σT) [S/cm] (x = 5)
1000	2.71	2.80	2.68	2.59	2.70
1200	2.77	2.78	2.84	2.78	2.77
1400	3.08	2.90	2.97	2.78	2.87
1600	3.18	3.04	2.97	2.86	2.91
1800	3.18	3.17	3.00	3.10	3.12
2000	3.29	3.19	3.099	2.90	3.21
2200	3.37	3.30	3.31	3.14	3.27
2500	3.53	3.34	3.37	3.12	3.22

The reported total conductivity and activation energy for Al-doped LLZO is 0.2-0.37 mS/cm [32], [91], [105], [103] and 0.34 eV [32], respectively which is also in agreement with the obtained results in this article. Almost all the Al-doped structures showed enhanced conductivity compared to undoped LLZO. On the contrary, Ga-doped LLZO enhanced the conductivity till the concentration for maximum conductivity is reached. Beyond the peak conductivity value, the Ga-doped structures showed less conductivity and activation energies than the undoped cubic LLZO structure.

Table 4.2. Temperature dependence of the conductivity obtained with AIMD simulation for Ga-doped LLZO structures ($Li_{7-3x}Ga_xLa_3Zr_2O_{12}$)

Temperature, T (K)	log(σT) [S/cm] (x = 1)	log(σT) [S/cm] (x = 2)	log(σT) [S/cm] (x = 3)	log(σT) [S/cm] (x = 4)	log(σT) [S/cm] (x = 5)
1000	2.795	2.62	2.75	2.57	2.51
1200	3.02	2.81	2.91	2.76	2.66
1400	3.00	2.83	2.93	2.89	2.60
1600	3.17	3.00	3.02	3.09	2.79
1800	3.24	3.05	3.18	3.05	3.06
2000	3.31	3.15	3.2	3.18	3.19
2200	3.51	3.25	3.23	3.34	3.08
2500	3.56	3.31	3.26	3.29	3.47

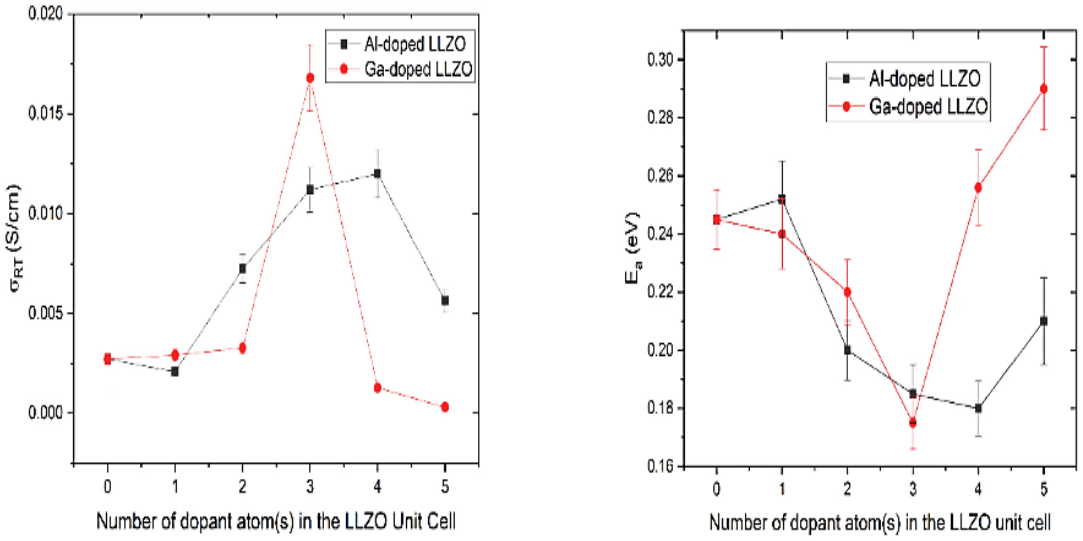

Figure 4.1. Dependency of (a) the room temperature conductivity, σ_{RT} and (b) the activation energy, E_a on the number of dopant(s) (i.e., Al/Ga) in the LLZO unit cell

4.3.2. Structural Stability

The thermodynamic stability of the Al-doped and Ga-doped LLZO compounds was also evaluated by the convex hull construction [106]. For the analysis, the energy of all known

compounds in the quaternary Li-M-La-Zr-O (M = Al, Ga) phase diagram was required. The stability results are listed in terms of energy above hull, ΔE Table 4.

Table 4.3. Energy above hull, ΔE of the Al-doped and Ga-doped cubic LLZO obtained for different dopant concentrations in the crystal unit cell.

Dopant	Composition	Energy Above Hull, ΔE (meV/atom)
Cubic undoped LLZO	$Li_7La_3Zr_2O_{12}$	11.63
Al	$Li_{6.625}Al_{0.125}La_3Zr_2O_{12}$	20.60
	$Li_{6.25}Al_{0.25}La_3Zr_2O_{12}$	21.27
	$Li_{5.875}Al_{0.375}La_3Zr_2O_{12}$	24.73
	$Li_{5.5}Al_{0.5}La_3Zr_2O_{12}$	24.84
	$Li_{5.125}Al_{0.625}La_3Zr_2O_{12}$	34.40
Ga	$Li_{6.625}Ga_{0.125}La_3Zr_2O_{12}$	21.40
	$Li_{6.25}Ga_{0.25}La_3Zr_2O_{12}$	22.86
	$Li_{5.875}Ga_{0.375}La_3Zr_2O_{12}$	24.60
	$Li_{5.5}Ga_{0.5}La_3Zr_2O_{12}$	28.58
	$Li_{5.125}Ga_{0.625}La_3Zr_2O_{12}$	29.27

All of the compounds in the $Li_{7-3x}M_xLa_3Zr_2O_{12}$ (M = Al, Ga) ($0 \leq x \leq 0.625$) series are predicted to be metastable with small ΔE (≤30 meV/atom) It is likely that the compounds remain synthesizable till their fastest ionic conductivity configuration, representing the optimal dopant content to achieve synthesizable compounds. A further increase in dopant concentration (i.e., Al/Ga) leads to the structure to become increasingly metastable ($\Delta E \geq 25$ meV/atom). This is a possible indication that the solubility of both Al-doped and Ga-doped LLZO may be limited.

4.4. Conclusion

In summary, the first-principles calculations were performed using the *ab initio* density functional theory to explore the effect of changing the dopant concentration on the total ionic

conductivity and structural stability in cubic LLZO. LLZO is one of the most promising materials used as solid electrolytes. For the improvement of its conductivity along with stability, understanding the effect of dopant concentration has appeared as a very important issue. We investigated the effect of changing the dopant concentration of $Li_{7-3x}M_xLa_3Zr_2O_{12}$ (M = Al, Ga) ($0 \leq x \leq 0.625$) on total ionic conductivity, activation energy, and structural stability of the doped LLZO. The computational results reported in this chapter confirms that the ionic conductivity and activation energy of doped LLZO have an observable dependency on the dopant contents in the LLZO unit cell. The conductivity vs. dopant concentration profile suggests that the conductivity increases with higher dopant (i.e., Al/Ga) concentration. The room temperature (30°C) ionic conductivity maximum and activation energy minimum for Al-doped and Ga-doped LLZO are seen for $Li_{5.5}Al_{0.5}La_3Zr_2O_{12}$ and $Li_{5.875}Ga_{0.375}La_3Zr_2O_{12}$ configurations, respectively. The room temperature conductivity and activation energy for $Li_{5.5}Al_{0.5}La_3Zr_2O_{12}$ have been calculated as 12 mS/cm and 0.18 eV, respectively. Similarly, for $Li_{5.875}Ga_{0.375}La_3Zr_2O_{12}$, the room temperature conductivity and activation energy have been calculated as 16.8 mS/cm and 0.18 eV, respectively. A further increase of dopant content from the threshold, as mentioned above, configurations leads to a decrease in conductivity and increases in activation energy. The stability study of the Al-doped and Ga-doped LLZO structures also suggests that the structures are also synthesizable till the threshold point of conductivity. A further increase in dopant content makes the synthesis of both Al-doped and Ga-doped LLZO difficult, and the material will be less stable arising from phase decomposition.

The ionic conductivity has been reinforced by the precise control over the crystal chemistry of the cubic LLZO garnet material. This enhancement of conductivity of LLZO material plays a vital role in their functionality in solid-state batteries. This work clearly provides a foundation for

the development of high-conducting ceramic electrolytes. This observation in our work can be extended towards the design of super-ionic electrolyte with optimal transport properties for inorganic conductors.

5. SUMMARY AND FUTURE WORK

5.1. Summary

Ab initio molecular dynamics (AIMD) simulation is widely used in studying the diffusion properties of materials. Garnet structured cubic LLZO crystal ($Li_{56}La_{24}Zr_{16}O_{96}$) is one of the most promising solid electrolytes for next-generation solid lithium-ion batteries owing to their high conductivity. In this work, the first-principles calculations were performed using the *ab initio* density functional theory to study the Li-ion diffusivity, room temperature conductivity, and phase stability of the garnet-type cubic LLZO material with varying lithium-ion concentration, ranging from 53 to 56 atoms (56 lithium atoms represent the stoichiometric concentration), and to explore the effect of changing the dopant concentration on the total ionic conductivity and structural stability in cubic LLZO(used as solid electrolytes). The computational results reported in this thesis confirm that the Li-ion self-diffusion has an observable dependency on the number of lithium atoms in the LLZO unit cell. The activation energy for the stoichiometric LLZO structure has been calculated as 0.25 eV. The increase in lithium vacancy concentration in LLZO leads to a decrease in activation energy. Furthermore, the phase stability of the cubic LLZO structures containing a different number of lithium atoms in the unit cell has also been calculated in terms of energy above hull at 0 K. The computational results reported in this dissertation demonstrate that with the removal of lithium atom from the LLZO unit cell, the structures gradually become more prone to decomposition, which indicates that the stoichiometric cubic LLZO structure is the most stable structure with energy above hull, ΔE = 11.63 meV/atom. The simulations suggest that if there is a reduction of the lithium atom number from the stoichiometric content (56 Li atoms), it will lead to the increase of room temperature (30°C) conductivity and the decrease of thermodynamic stability. Consequently, the effect of Al and Ga doping on the ionic conductivity

and stability of the garnet $Li_{7-3x}M_xLa_3Zr_2O_{12}$ (M = Al, Ga) ($0 \leq x \leq 0.625$) superionic conductor were also investigated. The computational results confirm that the ionic conductivity of LLZO increases with higher dopant (i.e., Al/Ga) concentration. An increase of dopant content beyond the threshold, leads to a decrease in conductivity and increases in activation energy. For the stability study also if the dopant is greater than the threshold point of conductivity, the synthesis of both Al-doped and Ga-doped LLZO will become difficult, and the material will be less stable arising from phase decomposition.

Overall, this study provides a valuable insight into the precise control over the crystal chemistry of the cubic LLZO garnet material for the improvement of ionic conductivity along with structural stability. This enhancement of conductivity of LLZO can be extended towards the design of super-ionic electrolytes with optimal transport properties for inorganic conductors.

5.2. Future Work

Garnet LLZO based materials are considered as one of the most promising solid electrolyte candidates for high ionic conductivity, safe and high energy density. To improve the performance and reliability of LLZO based materials, further study regarding the enhancement of conductivity and stability of the material is needed. A few possible directions are listed below:

- This dissertation revealed the relationship between conductivity and stability with the concentration of lithium vacancy defect and intentional additives (e.g., dopants such as Al and Ga). Further fundamental understanding of the Li-ion migration pathways, relevant chemical and electrochemical reactions, and compositional characteristics need to be deepened by advanced theoretical calculations.
- Besides, garnet LLZO materials have the potentiality to various lithium battery metal systems, such as Li-S, Li-V, and Li-air batteries, due to their unique properties. Further

studies can be performed in the future to benefit the development of these emerging lithium battery systems.

- Additionally, grain boundaries (GBs) are expected to have a large impact on Li-ion diffusion and conductivity properties. Continuation of this research toward the impact of GBs on Li-diffusion properties of pristine and doped LLZO should be considered in future studies.
- Finally, though AIMD simulations have emerged as a powerful tool for studying the ionic diffusivity and conductivity, it contains a couple of weaknesses. Of them, the significant computational cost compared to classical MD or other *ab initio* methods such as nudged elastic band calculations is a main weakness of AIMD. This weakness limits the computational materials system design on both spatial and temporal scales. Evaluating the macroscopic conductivity of LLZO based materials can be investigated in the future, accessing larger system sizes or time scales through the integration of AIMD with a force field and/or continuum methods in a multi-scale model.

REFERENCES

[1] A. Sharafi *et al.*, "Surface chemistry mechanism of ultra-low interfacial resistance in the solid-state electrolyte Li7La3Zr2O12," *Chem. Mater.*, vol. 29, no. 18, pp. 7961–7968, 2017.

[2] A. Sharafi *et al.*, "Impact of air exposure and surface chemistry on Li–Li 7 La 3 Zr 2 O 12 interfacial resistance," *J. Mater. Chem. A*, vol. 5, no. 26, pp. 13475–13487, 2017.

[3] T. Thompson *et al.*, "Electrochemical window of the Li-ion solid electrolyte Li7La3Zr2O12," *ACS Energy Lett.*, vol. 2, no. 2, pp. 462–468, 2017.

[4] S. Yu *et al.*, "Elastic properties of the solid electrolyte Li7La3Zr2O12 (LLZO)," *Chem. Mater.*, vol. 28, no. 1, pp. 197–206, 2015.

[5] S. Yu and D. J. Siegel, "Grain boundary contributions to Li-ion transport in the solid electrolyte Li7La3Zr2O12 (LLZO)," *Chem. Mater.*, vol. 29, no. 22, pp. 9639–9647, 2017.

[6] M. Armand and J.-M. Tarascon, "Building better batteries," *Nature*, vol. 451, no. 7179, p. 652, 2008.

[7] J.-M. Tarascon and M. Armand, "Issues and challenges facing rechargeable lithium batteries," in *Materials for Sustainable Energy: A Collection of Peer-Reviewed Research and Review Articles from Nature Publishing Group*, World Scientific, 2011, pp. 171–179.

[8] A. W. Golubkov *et al.*, "Thermal-runaway experiments on consumer Li-ion batteries with metal-oxide and olivin-type cathodes," *Rsc Adv.*, vol. 4, no. 7, pp. 3633–3642, 2014.

[9] X. Liu *et al.*, "Elucidating the mobility of H+ and Li+ ions in (Li 6.25− x H x Al 0.25) La 3 Zr 2 O 12 via correlative neutron and electron spectroscopy," *Energy Environ. Sci.*, vol. 12, no. 3, pp. 945–951, 2019.

[10] D. Aurbach *et al.*, "Review on electrode–electrolyte solution interactions, related to cathode materials for Li-ion batteries," *J. Power Sources*, vol. 165, no. 2, pp. 491–499, 2007.

[11] K. Amine, H. Tukamoto, H. Yasuda, and Y. Fujita, “Preparation and electrochemical investigation of LiMn2− xMexO4 (Me: Ni, Fe, and x= 0.5, 1) cathode materials for secondary lithium batteries,” *J. Power Sources*, vol. 68, no. 2, pp. 604–608, 1997.

[12] L. J. Miara *et al.*, “Effect of Rb and Ta Doping on the Ionic Conductivity and Stability of the Garnet Li7+ 2 x–y (La3–x Rb x)(Zr2–y Ta y) O12 (0≤ x≤ 0.375, 0≤ y≤ 1) Superionic Conductor: A First Principles Investigation,” *Chem. Mater.*, vol. 25, no. 15, pp. 3048–3055, 2013.

[13] A. Martínez-Juárez, C. Pecharromán, J. E. Iglesias, and J. M. Rojo, “Relationship between activation energy and bottleneck size for Li+ ion conduction in NASICON materials of composition LiMM ‘(PO4) 3; M, M ‘= Ge, Ti, Sn, Hf,” *J. Phys. Chem. B*, vol. 102, no. 2, pp. 372–375, 1998.

[14] A. R. Rodger, J. Kuwano, and A. R. West, “Li+ ion conducting γ solid solutions in the systems Li4XO4-Li3YO4: X= Si, Ge, Ti; Y= P, as, V; Li4XO4-LiZO2: Z= Al, Ga, Cr and Li4GeO4-Li2CaGeO4,” *Solid State Ionics*, vol. 15, no. 3, pp. 185–198, 1985.

[15] V. Thangadurai, S. Narayanan, and D. Pinzaru, “Garnet-type solid-state fast Li ion conductors for Li batteries: critical review,” *Chem. Soc. Rev.*, vol. 43, no. 13, pp. 4714–4727, 2014.

[16] H. Deiseroth *et al.*, “Li6PS5X: a class of crystalline Li-rich solids with an unusually high Li+ mobility,” *Angew. Chemie Int. Ed.*, vol. 47, no. 4, pp. 755–758, 2008.

[17] J. C. Bachman *et al.*, “Inorganic solid-state electrolytes for lithium batteries: mechanisms and properties governing ion conduction,” *Chem. Rev.*, vol. 116, no. 1, pp. 140–162, 2015.

[18] R. Kanno, T. Hata, Y. Kawamoto, and M. Irie, “Synthesis of a new lithium ionic conductor, thio-LISICON–lithium germanium sulfide system,” *Solid State Ionics*, vol. 130, no. 1–2, pp. 97–104, 2000.

[19] N. Kamaya *et al.*, “A lithium superionic conductor,” *Nat. Mater.*, vol. 10, no. 9, p. 682, 2011.

[20] S. P. Ong, Y. Mo, W. D. Richards, L. Miara, H. S. Lee, and G. Ceder, “Phase stability, electrochemical stability and ionic conductivity of the Li 10±1 MP 2 X 12 (M= Ge, Si, Sn, Al or P, and X= O, S or Se) family of superionic conductors,” *Energy Environ. Sci.*, vol. 6, no. 1, pp. 148–156, 2013.

[21] H. Muramatsu, A. Hayashi, T. Ohtomo, S. Hama, and M. Tatsumisago, “Structural change of Li2S–P2S5 sulfide solid electrolytes in the atmosphere,” *Solid State Ionics*, vol. 182, no. 1, pp. 116–119, 2011.

[22] X. Yao *et al.*, “All-solid-state lithium batteries with inorganic solid electrolytes: Review of fundamental science,” *Chinese Phys. B*, vol. 25, no. 1, p. 18802, 2015.

[23] K. Arbi, S. Mandal, J. M. Rojo, and J. Sanz, “Dependence of Ionic Conductivity on Composition of Fast Ionic Conductors Li1+ x Ti2-x Al x (PO4) 3, 0≤ x≤ 0.7. A Parallel NMR and Electric Impedance Study,” *Chem. Mater.*, vol. 14, no. 3, pp. 1091–1097, 2002.

[24] P. Hartmann *et al.*, “Degradation of NASICON-type materials in contact with lithium metal: formation of mixed conducting interphases (MCI) on solid electrolytes,” *J. Phys. Chem. C*, vol. 117, no. 41, pp. 21064–21074, 2013.

[25] P. Knauth, “Inorganic solid Li ion conductors: An overview,” *Solid State Ionics*, vol. 180, no. 14–16, pp. 911–916, 2009.

[26] O. Bohnke, “The fast lithium-ion conducting oxides Li3xLa2/3− xTiO3 from fundamentals to application,” *Solid State Ionics*, vol. 179, no. 1–6, pp. 9–15, 2008.

[27] V. Thangadurai and W. Weppner, “Recent progress in solid oxide and lithium ion conducting electrolytes research,” *Ionics (Kiel).*, vol. 12, no. 1, pp. 81–92, 2006.

[28] W. D. Richards, L. J. Miara, Y. Wang, J. C. Kim, and G. Ceder, “Interface stability in solid-state batteries,” *Chem. Mater.*, vol. 28, no. 1, pp. 266–273, 2015.

[29] C. Cao, Z.-B. Li, X.-L. Wang, X.-B. Zhao, and W.-Q. Han, “Recent advances in inorganic solid electrolytes for lithium batteries,” *Front. Energy Res.*, vol. 2, p. 25, 2014.

[30] M. Tatsumisago, M. Nagao, and A. Hayashi, “Recent development of sulfide solid electrolytes and interfacial modification for all-solid-state rechargeable lithium batteries,” *J. Asian Ceram. Soc.*, vol. 1, no. 1, pp. 17–25, 2013.

[31] Y. Zhu, X. He, and Y. Mo, “Origin of outstanding stability in the lithium solid electrolyte materials: insights from thermodynamic analyses based on first-principles calculations,” *ACS Appl. Mater. Interfaces*, vol. 7, no. 42, pp. 23685–23693, 2015.

[32] R. Murugan, V. Thangadurai, and W. Weppner, “Fast lithium ion conduction in garnet-type Li7La3Zr2O12,” *Angew. Chemie Int. Ed.*, vol. 46, no. 41, pp. 7778–7781, 2007.

[33] V. Thangadurai, H. Kaack, and W. J. F. Weppner, “Novel fast lithium ion conduction in garnet-type Li5La3M2O12 (M= Nb, Ta),” *J. Am. Ceram. Soc.*, vol. 86, no. 3, pp. 437–440, 2003.

[34] J. Awaka, N. Kijima, H. Hayakawa, and J. Akimoto, “Synthesis and structure analysis of tetragonal Li7La3Zr2O12 with the garnet-related type structure,” *J. Solid State Chem.*, vol. 182, no. 8, pp. 2046–2052, 2009.

[35] J. Percival, E. Kendrick, R. I. Smith, and P. R. Slater, "Cation ordering in Li containing garnets: synthesis and structural characterisation of the tetragonal system, Li 7 La 3 Sn 2 O 12," *Dalt. Trans.*, no. 26, pp. 5177–5181, 2009.

[36] K. Meier, T. Laino, and A. Curioni, "Solid-state electrolytes: revealing the mechanisms of Li-ion conduction in tetragonal and cubic LLZO by first-principles calculations," *J. Phys. Chem. C*, vol. 118, no. 13, pp. 6668–6679, 2014.

[37] D. O. Shin *et al.*, "Synergistic multi-doping effects on the Li 7 La 3 Zr 2 O 12 solid electrolyte for fast lithium ion conduction," *Sci. Rep.*, vol. 5, p. 18053, 2015.

[38] N. Bernstein, M. D. Johannes, and K. Hoang, "Origin of the structural phase transition in Li 7 La 3 Zr 2 O 12," *Phys. Rev. Lett.*, vol. 109, no. 20, p. 205702, 2012.

[39] E. J. Cussen, "Structure and ionic conductivity in lithium garnets," *J. Mater. Chem.*, vol. 20, no. 25, pp. 5167–5173, 2010.

[40] H. Xie, J. A. Alonso, Y. Li, M. T. Fernández-Díaz, and J. B. Goodenough, "Lithium distribution in aluminum-free cubic Li7La3Zr2O12," *Chem. Mater.*, vol. 23, no. 16, pp. 3587–3589, 2011.

[41] I. P. Roof, M. D. Smith, E. J. Cussen, and H.-C. zur Loye, "Crystal growth of a series of lithium garnets Ln3Li5Ta2O12 (Ln= La, Pr, Nd): Structural properties, Alexandrite effect and unusual ionic conductivity," *J. Solid State Chem.*, vol. 182, no. 2, pp. 295–300, 2009.

[42] B. Koch and M. Vogel, "Lithium ionic jump motion in the fast solid ion conductor Li5La3Nb2O12," *Solid State Nucl. Magn. Reson.*, vol. 34, no. 1–2, pp. 37–43, 2008.

[43] V. Thangadurai and W. Weppner, "Li6ALa2Ta2O12 (A= Sr, Ba): novel garnet-like oxides for fast lithium ion conduction," *Adv. Funct. Mater.*, vol. 15, no. 1, pp. 107–112, 2005.

[44] B. Andriyevsky, K. Doll, and T. Jacob, “Ab initio molecular dynamics study of lithium diffusion in tetragonal Li7La3Zr2O12,” *Mater. Chem. Phys.*, 2017.

[45] F. A. Garcia Daza, M. R. Bonilla, A. Llordés, J. Carrasco, and E. Akhmatskaya, “Atomistic Insight into Ion Transport and Conductivity in Ga/Al-Substituted Li7La3Zr2O12 Solid Electrolytes,” *ACS Appl. Mater. Interfaces*, vol. 11, no. 1, pp. 753–765, 2018.

[46] H. Buschmann *et al.*, “Structure and dynamics of the fast lithium ion conductor ‘Li 7 La 3 Zr 2 O 12,’” *Phys. Chem. Chem. Phys.*, vol. 13, no. 43, pp. 19378–19392, 2011.

[47] J. Wolfenstine, E. Rangasamy, J. L. Allen, and J. Sakamoto, “High conductivity of dense tetragonal Li7La3Zr2O12,” *J. Power Sources*, vol. 208, pp. 193–196, 2012.

[48] K. C. Santosh, R. C. Longo, K. Xiong, and K. Cho, “Point defects in garnet-type solid electrolyte (c-Li7La3Zr2O12) for Li-ion batteries,” *Solid State Ionics*, vol. 261, pp. 100–105, 2014.

[49] X. Zhan, S. Lai, M. P. Gobet, S. G. Greenbaum, and M. Shirpour, “Defect chemistry and electrical properties of garnet-type Li 7 La 3 Zr 2 O 12,” *Phys. Chem. Chem. Phys.*, vol. 20, no. 3, pp. 1447–1459, 2018.

[50] I. N. Levine, “Quantum chemistry, 4th Edition,” *J. Chem. Educ.*, 1993.

[51] M. Born and R. Oppenheimer, “Zur Quantentheorie der Molekeln,” *Ann. Phys.*, 1927.

[52] P. Hohenberg and W. Kohn, “Inhomogeneous Electron Gas Phys. Rev. 136,” *B864*, 1964.

[53] S. Yu, “Atomic Scale Simulations of the Solid Electrolyte Li7La3Zr2O12,” 2018.

[54] W. Kohn and L. J. Sham, “Self-consistent equations including exchange and correlation effects,” *Phys. Rev.*, 1965.

[55] M. Tuckerman, *Statistical mechanics: theory and molecular simulation*. Oxford university press, 2010.

[56] D. C. Rapaport and D. C. R. Rapaport, *The art of molecular dynamics simulation*. Cambridge university press, 2004.

[57] D. Marx and J. Hutter, *Ab initio molecular dynamics: basic theory and advanced methods*. Cambridge University Press, 2009.

[58] L. Verlet, “Computer" experiments" on classical fluids. I. Thermodynamical properties of Lennard-Jones molecules,” *Phys. Rev.*, vol. 159, no. 1, p. 98, 1967.

[59] W. C. Swope, H. C. Andersen, P. H. Berens, and K. R. Wilson, “A computer simulation method for the calculation of equilibrium constants for the formation of physical clusters of molecules: Application to small water clusters,” *J. Chem. Phys.*, vol. 76, no. 1, pp. 637–649, 1982.

[60] R. M. Martin and R. M. Martin, *Electronic structure: basic theory and practical methods*. Cambridge university press, 2004.

[61] G. Kresse and J. Furthmüller, “Efficient iterative schemes for ab initio total-energy calculations using a plane-wave basis set,” *Phys. Rev. B*, vol. 54, no. 16, p. 11169, 1996.

[62] P. E. Blöchl, “Projector augmented-wave method,” *Phys. Rev. B*, 1994.

[63] J. P. Perdew, M. Ernzerhof, and K. Burke, “Rationale for mixing exact exchange with density functional approximations,” *J. Chem. Phys.*, vol. 105, no. 22, pp. 9982–9985, 1996.

[64] P. P. Ewald, “Die Berechnung optischer und elektrostatischer Gitterpotentiale,” *Ann. Phys.*, vol. 369, no. 3, pp. 253–287, 1921.

[65] S. P. Ong *et al.*, “Python Materials Genomics (pymatgen): A robust, open-source python library for materials analysis,” *Comput. Mater. Sci.*, vol. 68, pp. 314–319, 2013.

[66] J. Awaka, A. Takashima, K. Kataoka, N. Kijima, Y. Idemoto, and J. Akimoto, "Crystal structure of fast lithium-ion-conducting cubic Li7La3Zr2O12," *Chem. Lett.*, vol. 40, no. 1, pp. 60–62, 2010.

[67] T. Róg, K. Murzyn, K. Binsen, and G. R. Kneller, "Software news and updates nMoldyn: A program package for a neutron scattering oriented analysis of Molecular Dynamics simulations," *J. Comput. Chem.*, 2003.

[68] X. He, Y. Zhu, A. Epstein, and Y. Mo, "Statistical variances of diffusional properties from ab initio molecular dynamics simulations," *npj Comput. Mater.*, 2018.

[69] P. Heitjans and S. Indris, "Diffusion and ionic conduction in nanocrystalline ceramics," *J. Phys. Condens. Matter*, vol. 15, no. 30, p. R1257, 2003.

[70] Q. Bai, X. He, Y. Zhu, and Y. Mo, "First-Principles Study of Oxyhydride H– Ion Conductors: Toward Facile Anion Conduction in Oxide-Based Materials," *ACS Appl. Energy Mater.*, vol. 1, no. 4, pp. 1626–1634, Apr. 2018.

[71] Z. Deng, Z. Zhu, I.-H. Chu, and S. P. Ong, "Data-Driven First-Principles Methods for the Study and Design of Alkali Superionic Conductors," *Chem. Mater.*, vol. 29, no. 1, pp. 281–288, Jan. 2017.

[72] M. Landstorfer and T. Jacob, "Mathematical modeling of intercalation batteries at the cell level and beyond," *Chem. Soc. Rev.*, vol. 42, no. 8, pp. 3234–3252, 2013.

[73] M. Landstorfer, S. Funken, and T. Jacob, "An advanced model framework for solid electrolyte intercalation batteries," *Phys. Chem. Chem. Phys.*, vol. 13, no. 28, pp. 12817–12825, 2011.

[74] N. J. J. de Klerk, E. van der Maas, and M. Wagemaker, "Analysis of Diffusion in Solid-State Electrolytes through MD Simulations, Improvement of the Li-Ion Conductivity in β-Li3PS4 as an Example," *ACS Appl. Energy Mater.*, vol. 1, no. 7, pp. 3230–3242, Jul. 2018.

[75] L. J. Miara *et al.*, "Effect of Rb and Ta Doping on the Ionic Conductivity and Stability of the Garnet Li7+2x–y(La3–xRbx)(Zr2–yTay)O12 ($0 \leq x \leq 0.375$, $0 \leq y \leq 1$) Superionic Conductor: A First Principles Investigation," *Chem. Mater.*, vol. 25, no. 15, pp. 3048–3055, Aug. 2013.

[76] J. Gao *et al.*, "The Ab Initio Calculations on the Areal Specific Resistance of Li-Metal/Li7La3Zr2O12 Interphase," *Adv. Theory Simulations*, vol. 2, no. 6, p. 1900028, 2019.

[77] S. R. Yeandel, B. J. Chapman, P. R. Slater, and P. Goddard, "Structure and lithium-ion dynamics in fluoride-doped cubic Li7La3Zr2O12 (LLZO) garnet for Li solid-state battery applications," *J. Phys. Chem. C*, vol. 122, no. 49, pp. 27811–27819, 2018.

[78] S. Baek, J.-M. Lee, T. Y. Kim, M.-S. Song, and Y. Park, "Garnet related lithium ion conductor processed by spark plasma sintering for all solid state batteries," *J. Power Sources*, vol. 249, pp. 197–206, 2014.

[79] J. Sakamoto, E. Rangasamy, H. Kim, Y. Kim, and J. Wolfenstine, "Synthesis of nano-scale fast ion conducting cubic Li7La3Zr2O12," *Nanotechnology*, vol. 24, no. 42, p. 424005, 2013.

[80] S. Adams and R. P. Rao, "Ion transport and phase transition in Li 7− x La 3 (Zr 2− x M x) O 12 (M= Ta 5+, Nb 5+, x= 0, 0.25)," *J. Mater. Chem.*, vol. 22, no. 4, pp. 1426–1434, 2012.

[81] H. Buschmann *et al.*, "Structure and dynamics of the fast lithium ion conductor" Li7La3Zr2O12"(vol 13, pg 19378, 2011)," *Phys. Chem. Chem. Phys.*, vol. 13, no. 48, pp. 21658–21659, 2011.

[82] A. Kuhn, S. Narayanan, L. Spencer, G. Goward, V. Thangadurai, and M. Wilkening, "Li self-diffusion in garnet-type Li 7 La 3 Zr 2 O 12 as probed directly by diffusion-induced Li 7 spin-lattice relaxation NMR spectroscopy," *Phys. Rev. B*, vol. 83, no. 9, p. 94302, 2011.

[83] C. Shao, H. Liu, Z. Yu, Z. Zheng, N. Sun, and C. Diao, "Structure and ionic conductivity of cubic Li7La3Zr2O12 solid electrolyte prepared by chemical co-precipitation method," *Solid State Ionics*, vol. 287, pp. 13–16, 2016.

[84] Y. Zhu, X. He, and Y. Mo, "First principles study on electrochemical and chemical stability of solid electrolyte-electrode interfaces in all-solid-state Li-ion batteries," *J. Mater. Chem. A*, 2016.

[85] M. Huang *et al.*, "Effect of sintering temperature on structure and ionic conductivity of Li7− xLa3Zr2O12− 0.5 x (x= 0.5~ 0.7) ceramics," *Solid State Ionics*, vol. 204, pp. 41–45, 2011.

[86] S. Ohta, T. Kobayashi, and T. Asaoka, "High lithium ionic conductivity in the garnet-type oxide Li7− X La3 (Zr2− X, NbX) O12 (X= 0–2)," *J. Power Sources*, vol. 196, no. 6, pp. 3342–3345, 2011.

[87] S. Kumazaki *et al.*, "High lithium ion conductive Li7La3Zr2O12 by inclusion of both Al and Si," *Electrochem. commun.*, vol. 13, no. 5, pp. 509–512, 2011.

[88] S. Ohta, J. Seki, Y. Yagi, Y. Kihira, T. Tani, and T. Asaoka, "Co-sinterable lithium garnet-type oxide electrolyte with cathode for all-solid-state lithium ion battery," *J. Power Sources*, vol. 265, pp. 40–44, 2014.

[89] M. Kotobuki, K. Kanamura, Y. Sato, and T. Yoshida, "Fabrication of all-solid-state lithium battery with lithium metal anode using Al2O3-added Li7La3Zr2O12 solid electrolyte," *J. Power Sources*, vol. 196, no. 18, pp. 7750–7754, 2011.

[90] Y. Li, C.-A. Wang, H. Xie, J. Cheng, and J. B. Goodenough, “High lithium ion conduction in garnet-type Li6La3ZrTaO12,” *Electrochem. commun.*, vol. 13, no. 12, pp. 1289–1292, 2011.

[91] Y. Jin and P. J. McGinn, “Al-doped Li7La3Zr2O12 synthesized by a polymerized complex method,” *J. Power Sources*, vol. 196, no. 20, pp. 8683–8687, 2011.

[92] M. Kotobuki, H. Munakata, K. Kanamura, Y. Sato, and T. Yoshida, “Compatibility of Li7La3Zr2O12 solid electrolyte to all-solid-state battery using Li metal anode,” *J. Electrochem. Soc.*, vol. 157, no. 10, pp. A1076–A1079, 2010.

[93] J. L. Allen, J. Wolfenstine, E. Rangasamy, and J. Sakamoto, “Effect of substitution (Ta, Al, Ga) on the conductivity of Li7La3Zr2O12,” *J. Power Sources*, vol. 206, pp. 315–319, 2012.

[94] R. Wagner *et al.*, “Crystal structure of garnet-related Li-ion conductor Li7–3 x Ga x La3Zr2O12: fast Li-ion conduction caused by a different cubic modification?,” *Chem. Mater.*, vol. 28, no. 6, pp. 1861–1871, 2016.

[95] D. Rettenwander, C. A. Geiger, M. Tribus, P. Tropper, and G. Amthauer, “A Synthesis and Crystal Chemical Study of the Fast Ion Conductor Li7–3 x Ga x La3 Zr2O12 with x= 0.08 to 0.84,” *Inorg. Chem.*, vol. 53, no. 12, pp. 6264–6269, 2014.

[96] H. El Shinawi and J. Janek, “Stabilization of cubic lithium-stuffed garnets of the type ‘Li7La3Zr2O12’ by addition of gallium,” *J. Power Sources*, vol. 225, pp. 13–19, 2013.

[97] J. Wolfenstine, J. Ratchford, E. Rangasamy, J. Sakamoto, and J. L. Allen, “Synthesis and high Li-ion conductivity of Ga-stabilized cubic Li7La3Zr2O12,” *Mater. Chem. Phys.*, vol. 134, no. 2–3, pp. 571–575, 2012.

[98] R. Jalem *et al.*, “Effects of gallium doping in garnet-type Li7La3Zr2O12 solid electrolytes,” *Chem. Mater.*, vol. 27, no. 8, pp. 2821–2831, 2015.

[99] D. Wang *et al.*, "The synergistic effects of Al and Te on the structure and Li+-mobility of garnet-type solid electrolytes," *J. Mater. Chem. A*, vol. 2, no. 47, pp. 20271–20279, 2014.

[100] M. Huang, M. Shoji, Y. Shen, C.-W. Nan, H. Munakata, and K. Kanamura, "Preparation and electrochemical properties of Zr-site substituted Li7La3 (Zr2− xMx) O12 (M= Ta, Nb) solid electrolytes," *J. Power Sources*, vol. 261, pp. 206–211, 2014.

[101] Y. Li, J.-T. Han, C.-A. Wang, H. Xie, and J. B. Goodenough, "Optimizing Li+ conductivity in a garnet framework," *J. Mater. Chem.*, vol. 22, no. 30, pp. 15357–15361, 2012.

[102] Y. Li *et al.*, "W-doped Li7La3Zr2O12 ceramic electrolytes for solid state Li-ion batteries," *Electrochim. Acta*, vol. 180, pp. 37–42, 2015.

[103] C. A. Geiger *et al.*, "Crystal chemistry and stability of 'Li7La3Zr2O12' garnet: a fast lithium-ion conductor," *Inorg. Chem.*, vol. 50, no. 3, pp. 1089–1097, 2011.

[104] J.-F. Wu *et al.*, "Gallium-doped Li7La3Zr2O12 garnet-type electrolytes with high lithium-ion conductivity," *ACS Appl. Mater. Interfaces*, vol. 9, no. 2, pp. 1542–1552, 2017.

[105] I. N. David, T. Thompson, J. Wolfenstine, J. L. Allen, and J. Sakamoto, "Microstructure and Li-Ion Conductivity of Hot-Pressed Cubic Li7La3Zr2O12," *J. Am. Ceram. Soc.*, vol. 98, no. 4, pp. 1209–1214, 2015.

[106] T. J. Marrone, and Briggs James M, and J. A. McCammon, "Structure-based drug design: computational advances," *Annu. Rev. Pharmacol. Toxicol.*, vol. 37, no. 1, pp. 71–90, 1997.

APPENDIX A. ADDITIONAL INFORMATION

Table A.1. Temperature dependence of the diffusivity obtained with AIMD simulation for LLZO structures with Lithium Defects

Temperature	ln(D) [cm^2/s] $Li_7La_3Zr_2O_{12}$	ln(D) [cm^2/s] $Li_{6.875}La_3Zr_2O_{12}$	ln(D) [cm^2/s] $Li_{6.75}La_3Zr_2O_{12}$	ln(D) [cm^2/s] $Li_{6.625}La_3Zr_2O_{12}$
1000	-11.2428	-10.87409	-10.751	-10.839
1200	-10.7807	-10.65736186	-10.6281	-10.7082
1400	-10.6372	-10.51314	-10.5855	-10.5825
1600	-10.4036	-10.31501098	-10.1742	-10.1444
1800	-10.1242	-10.18941117	-10.1569	-9.96511
2000	-10.0398	-10.11566644	-9.93273	-9.86596
2200	-9.94861	-9.782722301	-9.62383	-9.87166
2500		-9.562568077	-9.55791	-9.52249

Table A.2. Temperature dependence of the diffusivity obtained with AIMD simulation for LLZO structures with Lithium Defects

Temperature	$\log(\sigma T)$ [S/cm] $Li_7La_3Zr_2O_{12}$	$\log(\sigma T)$ [S/cm] $Li_{6.875}La_3Zr_2O_{12}$	$\log(\sigma T)$ [S/cm] $Li_{6.75}La_3Zr_2O_{12}$	$\log(\sigma T)$ [S/cm] $Li_{6.625}La_3Zr_2O_{12}$
1000	2.794724997	2.990467614	2.992553518	2.9462213
1200	2.995445643	3.041162053	3.045895401	3.002989791
1400	3.057754323	3.181877873	3.064394338	3.057578628
1600	3.159196501	3.18984726	3.243018195	3.24787511
1800	3.280537397	3.244392917	3.25053466	3.325716755
2000	3.317185508	3.276429633	3.347915187	3.368807354
2200	3.356817197	3.421024481	3.482049929	3.366292182
2500		3.516634517	3.510679031	3.517954261

Table A.3. Temperature dependence of the diffusivity obtained with AIMD simulation for Al-doped LLZO structures ($Li_{7-3x}Al_xLa_3Zr_2O_{12}$)

Tempe-rature	ln(D) [cm^2/s] (x = 0)	ln(D) [cm^2/s] (x = 1)	ln(D) [cm^2/s] (x = 2)	ln(D) [cm^2/s] (x = 3)	ln(D) [cm^2/s] (x = 4)	ln(D) [cm^2/s] (x = 5)
1000	-11.24	-11.383	-11.113	-11.343	-11.4687	-11.144
1200	-10.78	-11.255	-11.146	-10.969	-11.044	-10.988
1400	-10.63	-10.512	-10.886	-10.673	-11.041	-10.755
1600	-10.40	-10.290	-10.543	-10.665	-10.859	-10.670
1800	-10.12	-10.290	-10.254	-10.577	-10.298	-10.176
2000	-10.04	-10.029	-10.201	-10.366	-10.749	-9.967
2200	-9.95	-9.861	-9.961	-9.872	-10.199	-9.837
2500		-9.502	-9.873	-9.736	-10.25	-9.941

Table A.4. Temperature dependence of the diffusivity obtained with AIMD simulation for Ga-doped LLZO structures ($Li_{7-3x}Ga_xLa_3Zr_2O_{12}$)

Temperature	ln(D) [cm^2/s] (x = 0)	ln(D) [cm^2/s] (x = 1)	ln(D) [cm^2/s] (x = 2)	ln(D) [cm^2/s] (x = 3)	ln(D) [cm^2/s] (x = 4)	ln(D) [cm^2/s] (x = 5)
1000	-11.242	-11.185	-11.524	-11.159	-11.526	-11.585
1200	-10.780	-10.672	-11.086	-10.797	-11.092	-11.230
1400	-10.637	-10.706	-11.043	-10.752	-10.783	-11.378
1600	-10.403	-10.317	-10.648	-10.538	-10.311	-10.943
1800	-10.124	-10.155	-10.544	-10.182	-10.412	-10.316
2000	-10.039	-10.011	-10.315	-10.136	-10.125	-10.001
2200	-9.948	-9.547	-10.085	-10.061	-9.733	-10.264
2500		-9.436	-9.942	-9.992	-9.852	-9.374

APPENDIX B. VASP INPUT FILES

B.1. Geometrical Relaxation of Crystal Structures

SYSTEM = LLZO

PREC = Normal

ALGO = Fast # Fast, Normal, All

IWAVPR = 11

ISTART = 1 # job : 0-new 1-cont 2-samecut

ICHARG = 1 # means reading charge density from CHGCAR and keep constant during the subsequent run

EDIFF= 1.0E-5 # stopping-criterion for ELM

ENCUT = 400 # ENMAX in POTCAR

NELM = 60 # max number of selfconsistance steps, 40 normally

NELMIN = 4 # min number of SC steps

NELMDL = 10

NBLOCK = 1 ; KBLOCK = 1000 # default =1

EDIFFG = 1E-3 #stopping-criterion for IOM

IBRION = 2 # -1 if NSW=1,0 ,0 for MD, 1 for newton, 2 for conj-grad

NSW = 900 # max number of steps for IOM

ISIF = 2 # 3=full vol relax, 2=no vol or shape change

ISMEAR = 0 #determines how the partial occupancies

ISPIN = 1 # non-spin polarized calculation

SIGMA = 0.2 # 0.1 or 0.05 can also be used to find minimum energy structure

ISYM = 0 #switch of symmetry, for MD

NPAR = 4 # number of nodes to use, Necessary to get all information when running in parallel

LPLANE = .TRUE. # good for large cells

LSCALU=.FALSE.

LSCALAPACK = .TRUE.

LREAL = Auto # projection in real space, keep false always

LWAVE = .TRUE. # determines if WAVECAR is written

LCHARG = .TRUE.

LASPH=.TRUE. # cheap and adds some corrections to energy

B.2. Heating an Crystal Structure

SYSTEM = LLZO

ALGO = Fast

LREAL = Auto

NSIM = 4

MAXMIX = 20

LPLANE=.TRUE.

LASPH=.TRUE.

NPAR = 4

BMIX = 1

EDIFF = 1e-05

IBRION = 0

ICHARG = 0

ISIF = 0

ISMEAR = 0

ISPIN = 1

ISYM = 0

KBLOCK = 100

LCHARG = False

LORBIT = 11

LSCALU = False

LWAVE = .TRUE.

NBLOCK = 1

NELM = 60

NELMIN = 4

NSW = 1000

POTIM = 1

PREC = Normal

SIGMA = 0.05

SMASS = -1

TEBEG = 10

TEEND = *Temp*

B.3. NVT Operation

ALGO = Fast

BMIX = 1

IBRION = 0

ICHARG = 0

ISYM = 0

ISMEAR = 0

ISPIN = 1

KBLOCK = 100

LCHARG = False

LORBIT = 11

LPLANE = True

LREAL = Auto

LSCALU = False

LWAVE = False

MAXMIX = 50

NBLOCK = 1

NELM = 1000

NELMIN = 4

NSIM = 4

NSW = 20000

POTIM = 1

PREC = Normal

SIGMA = 0.05

SMASS = 0

TEBEG = **Temp**

TEEND = **Temp**

NPAR = 4

LMAXMIX = 4

APPENDIX C. PYTHON CODES

The python codes used in this study are presented below.

C.1. Convert Symmetry CIF to Numerical CIF

```
"""
Created on Thu Nov  1 14:55:37 2018

@author: Sudipto
"""

from pymatgen.io.cif import CifParser
path="/directory/cif Files/"
file_name ="ABCD.cif"

struct=CifParser(path+file_name,occupancy_tolerance=2.0).get_structures(primitive = False)[0]
struct.to("cif",path+"new llzo-5.cif")
```

C.2. Random Structure Generation

C.2.1. Main File

```
import re
import random

class main1():

    num_Li=0
    num_otherelements=0
    Li_info= dict()
    otherelements_info= dict()
    to_write_random= dict()
    to_write_otherelements= dict()
    num_random_Li=0
    num_random_otherelements=0

    #creating two dict for first 24 and next 96 elements
    first_bundle = dict()
    second_bundle = dict()

    def __init__(self, input_file, outfile):
        self.input_file = input_file
        self.outfile = outfile
        self._process_netlist()
```

```
    def _process_netlist(self):
        """Process the netlist file to identify the necessary components"""
        with open(self.input_file, 'r') as input_file:
            lines = input_file.readlines()
            for i in range(1,len(lines)):
                if i > 31:
                    (element, others) = lines[i].split('      ',1)
                    element= element.rstrip()
#                     print (element)
#                     print(others)
                    mat1= re.search (r'(?P<var>[A-z]+)[0-9]+.*',element)
                    m= mat1.group('var')
                    #print (m)
                    if m== 'Li':
                        self.num_Li+=1
                        self.Li_info[self.num_Li]= dict()
                        self.Li_info[self.num_Li]['element']= element
                        self.Li_info[self.num_Li]['other']= others

                        if self.num_Li<=24:
                                self.first_bundle[self.num_Li] = dict()
                                self.first_bundle[self.num_Li]['element']= element
                                self.first_bundle[self.num_Li]['other']= others
                        else:
                                self.second_bundle[self.num_Li] = dict()
                                self.second_bundle[self.num_Li]['element']= element
                                self.second_bundle[self.num_Li]['other']= others
                    else:
                        self.num_otherelements+=1
                        self.otherelements_info[self.num_otherelements]= dict()
                        self.otherelements_info[self.num_otherelements]['element']= element
                        self.otherelements_info[self.num_otherelements]['other']= others
#                         print (self.otherelements_info[self.num_otherelements]['element'])

#             for x in range (1,57):
#                 self.num_random_Li+=1
#                 self.to_write_random[x] = dict()
#                 k= random.choice(list(self.Li_info))
#                 self.to_write_random[x]['element']= self.Li_info[k]['element']
#                 self.to_write_random[x]['others']= self.Li_info[k]['other']
#                 self.Li_info.pop(k)
#                     print(self.to_write_random['element'])
#                 x=x+1

            for x in range (1,57):
                self.num_random_Li+=1
```

```
            self.to_write_random[x] = dict()
            if x<24:
              k= random.choice(list(self.first_bundle))
              self.to_write_random[x]['element']= self.first_bundle[k]['element']
              self.to_write_random[x]['others']= self.first_bundle[k]['other']
              self.first_bundle.pop(k)
            else:
              k= random.choice(list(self.second_bundle))
              self.to_write_random[x]['element']= self.second_bundle[k]['element']
              self.to_write_random[x]['others']= self.second_bundle[k]['other']
              self.second_bundle.pop(k)
#             x=x+1


    def Li_struc(self,x):
        """Returns the declarations of the Li elements"""
        return (self.to_write_random[x]['element']) +'     ' + (self.to_write_random[x]['others'])
    def otherelements_struc(self,x):
        """Returns the declarations of the other elements"""
        return (self.otherelements_info[x]['element']) +'     ' + (self.otherelements_info[x]['other'])
    def generate_file(self):
        """write the final file to the output file"""
        with open(self.input_file, 'r') as input_file:
            with open(self.outfile, 'w') as out_file:
                i=0
                lines = input_file.readlines()
    #               print(len(lines))
                while i < 32:
                    out_file.write(lines[i])
                    i=i+1
                for x in range (1, self.num_random_Li+1):
                    out_file.write(self.Li_struc(x))
                for x in range (1, self.num_otherelements+1):
                    out_file.write(self.otherelements_struc(x))
```

C.2.2. Run File

```
"""Main script used to generate, run, and record execution time of smt2 proofs"""

import os
import sys
import time
#from time import sleep
```

```
from main import main1


start = time.time()

def main():
    """Main function"""
    print ('Print information here')
    i = 1
    max_i = 2
    while (i <= max_i):
        Object = main1('Cubic.txt', 'Random'+str(i)+'.cif')
        Object.generate_file()
        i+=1
#       sleep(0.1)

if __name__ == '__main__':
    main()

end = time.time()

#print(end-start)
```

C.3. Removing Lithium by Combination

C.3.1. Main File

```
import re
import random

class _generator():

    num_Li=0
    num_otherelements=0
    Li_info= dict()
    otherelements_info= dict()
    to_write_random= dict()
    to_write_otherelements= dict()
    num_random_Li=0
    num_random_otherelements=0

    #creating two dict for first 24 and next 96 elements
    first_bundle = dict()
    second_bundle = dict()

    def __init__(self, input_file, outfile, list_2_rem):
        self.input_file = input_file
```

```
        self.outfile = outfile
        self.list_2_rem = list(list_2_rem)
        self._process_netlist()

    def _process_netlist(self):
        """Process the netlist file to identify the necessary components"""
        with open(self.input_file, 'r') as input_file:
            lines = input_file.readlines()
            for i in range(1,len(lines)):
                if i > 31:
                    (element, others) = lines[i].split('      ',1)
                    element= element.rstrip()
#                     print (element)
#                     print(others)
                    mat1= re.search (r'(?P<var>[A-z]+)[0-9]+.*',element)
                    m= mat1.group('var')
                    #print (m)
                    if m== 'Li':
                        self.num_Li+=1
                        self.Li_info[self.num_Li]= dict()
                        self.Li_info[self.num_Li]['element']= element
                        self.Li_info[self.num_Li]['other']= others
                    else:
                        self.num_otherelements+=1
                        self.otherelements_info[self.num_otherelements]= dict()
                        self.otherelements_info[self.num_otherelements]['element']= element
                        self.otherelements_info[self.num_otherelements]['other']= others
#                         print (self.otherelements_info[self.num_otherelements]['element'])

#             for x in range (1,57):
#                 self.num_random_Li+=1
#                 self.to_write_random[x] = dict()
#                 k= random.choice(list(self.Li_info))
#                 self.to_write_random[x]['element']= self.Li_info[k]['element']
#                 self.to_write_random[x]['others']= self.Li_info[k]['other']
#                 self.Li_info.pop(k)
#                     print(self.to_write_random['element'])
#                 x=x+1

            #for i in self.list_2_rem:
            #    self.Li_info.pop(i)
            #    self.num_Li = self.num_Li-1

    def _filter(self, x):
        for i in self.list_2_rem:
            #print()
```

```
        if (x==i):
            return 1
    return 0

def Li_struc(self, x):
    """Returns the declarations of the Li elements"""
    return (self.Li_info[x]['element']) +'     ' + (self.Li_info[x]['other'])

def otherelements_struc(self,x):
    """Returns the declarations of the other elements"""
    return (self.otherelements_info[x]['element']) +'     ' + (self.otherelements_info[x]['other'])

def generate_file(self):
    """write the final file to the output file"""
    with open(self.input_file, 'r') as input_file:
        with open(self.outfile, 'w') as out_file:
            i=0
            lines = input_file.readlines()
#               print(len(lines))
            while i < 32:
                out_file.write(lines[i])
                i=i+1
            for x in range (1, self.num_Li+1):
                if(self._filter(x)==0):
                    out_file.write(self.Li_struc(x))

            for x in range (1, self.num_otherelements+1):
                out_file.write(self.otherelements_struc(x))
```

C.3.2. Run File

```
import os
if not os.path.exists('output'):
    os.makedirs('output')

import sys
import time
#from time import sleep
import itertools as it

from main import _generator


start = time.time()
file_num = 1
def main():
```

```
    """Main function"""
    global file_num
    print ('Assuming main file: mother_file.cif')
    print ('Assuming 56 Li elements')
    _no = int(input('Enter the number of Li to be eliminated: '))

    removal_list = list(it.combinations(range(1,57),_no))

    for i in removal_list:
        Object = _generator('cubic_mother_file.txt', 'output/'+'output'+str(file_num)+'.cif',list(i))
        Object.generate_file()
        file_num = file_num + 1

if __name__ == '__main__':
    main()

end = time.time()

#print(end-start)
```

C.4. Ewald Energy Calculation

```
"""
Created on Thu November 15 10:54:42 2018

@author: sudipto.saha
"""
import warnings
warnings.filterwarnings("ignore")
import os
from pymatgen.io.cif import CifParser
from pymatgen.core import Structure
from pymatgen.analysis import ewald

# To read the cif file and create structure #
path="/Directory/"
file_name = "output"
file_ext = ".cif"

# for storing the results
energy = []
file_no = []
_no_file = 15000
```

```
def get_edwald_energy(fl):
        print ("Reading file", format(file_name + str(fl) + file_ext))
        struct=CifParser( path + file_name + str(fl) + file_ext,
occupancy_tolerance=1.0).get_structures(primitive = False)[0]
        struct.add_oxidation_state_by_element({"Li":1,"La":3,"Al":3,"Ga":3,"Sc":3,"Y":3,"B
a":  2,"Zr":4,"Yb":  3,  "Fe":4,"Ti":  4,  "O":  -2,"H":  1,"In":
3,"Cu":2,"Na":1,"Co":3,"Sr":2,"Ni":3,"Sm":3})
        #energy calculation
        call_the_class=ewald.EwaldSummation(struct)
        Ewald_Energy=call_the_class.total_energy
        return Ewald_Energy

for i in range (1,_no_file+1):
        energy.append(get_edwald_energy(i))
        file_no.append(format(file_name + str(i) + file_ext))

print ("\nPrimary output\n")

for i in range (0,_no_file):
        print (file_no[i], " ", energy[i])

print ("\nSorting the data")

for i in range (0,_no_file):
        for j in range(i,_no_file):
            if energy[j] < energy[i]:       #swap
                tmp_val = energy[i]
                tmp_no = file_no[i]

                energy[i] = energy[j]
                file_no[i] = file_no[j]

                energy[j] = tmp_val
                file_no[j] = tmp_no

print ("\nGenerating sorted output\n")

file = open("Ga_5 Ewald Energy.txt","w")

for i in range (0,_no_file):
        print (file_no[i], " ", energy[i])
        file.write(str(file_no[i]+" "+str(energy[i])+"\n"))

file.close()
```

C.5. Energy Above Hull Calculation

```
from pymatgen import MPRester
from pymatgen.io.vasp.outputs import Vasprun,Outcar
from pymatgen.entries.compatibility import MaterialsProjectCompatibility
from pymatgen.analysis.phase_diagram import PhaseDiagram,PDPlotter
#from pymatgen.phasediagram.plotter import PDPlotter
import argparse
from pymatgen.io.vasp.sets import MPRelaxSet
from pymatgen.core.structure import Structure
import os
import shutil

vasprun=Vasprun("E:/Research/2018/e_above_hull/CLR/55Li/vasprun.xml")
new_uncorrected_entry =
vasprun.get_computed_entry(inc_structure=True,parameters=[],data=[])
MPCompatibility = MaterialsProjectCompatibility() #energy correction
new_entry = MPCompatibility.process_entry(new_uncorrected_entry)
struct = new_entry.structure
struct.remove_oxidation_states()
elements = [str(i) for i in struct.types_of_specie]
entries =MPRester('qgm4xgbIeCJ7tS1qd3').get_entries_in_chemsys(elements) #from
pymatgen.matproj.rest import MPRester
pd=PhaseDiagram(entries) #from pymatgen.phasediagram.maker import
GrandPotentialPhaseDiagram, PhaseDiagram
# pda=PDAnalyzer(pd) #from pymatgen.phasediagram.analyzer import PDAnalyzer
decomp_entries,e_above_hull =
pd.get_decomp_and_e_above_hull(new_entry,allow_negative=True)

ehull = e_above_hull * 1000

if ehull < 1:
   print("Entry is stable.")
elif ehull < 30:
      print ("Entry is metastable and could be stable at finite temperatures.")
elif ehull < 50:
      print ("Entry has a low probability of being stable.")
else:
      print ("Entry is very unlikely to be stable.")
print (e_above_hull)
#print (decomp_entries)

print ('Stable Entries (formula, materials_id)\n--------')
for e in pd.stable_entries:
 print (e.composition.reduced_formula, e.entry_id)
```

```
print ( '\nUnstable Entries (formula, materials_id, e_above_hull (eV/atom), decomposes_to)\n----------')
for e in pd.unstable_entries:
 decomp, e_above_hull = pd.get_decomp_and_e_above_hull(e)
 pretty_decomp = [("{}:{}".format(k.composition.reduced_formula, k.entry_id), round(v, 2)) for k, v in decomp.items()]
 print ( e.composition.reduced_formula, e.entry_id, "%.3f" % e_above_hull, pretty_decomp)

# Plot!
plotter = PDPlotter(pd, show_unstable=False)  # you can also try show_unstable=True
plotter.show()
plotter.write_image("AA.png".format('-'.join(system)), "png")  # save figure
```

C.6. Doping Lithium Site With Single Element

C.6.1. Main file

```
import re
import random

class _generator():

    num_Li=0
    num_otherelements=0
    Li_info= dict()
    otherelements_info= dict()
    to_write_random= dict()
    to_write_otherelements= dict()
    num_random_Li=0
    num_random_otherelements=0
    head_no = 0
    #creating two dict for first 24 and next 96 elements
    first_bundle = dict()
    second_bundle = dict()

    def __init__(self, input_file, outfile, list_2_rem, list_2_ren,n_name):
        self.input_file = input_file
        self.outfile = outfile
        self.list_2_rem = list(list_2_rem)
        self.list_2_ren = list(list_2_ren)
        self.n_name = n_name
        self._process_netlist()

    def _process_netlist(self):
        insert_element = False
        """Process the netlist file to identify the necessary components"""
        with open(self.input_file, 'r') as input_file:
```

```
        lines = input_file.readlines()
        for i in range(1,len(lines)):
            #print(insert_element)
            if insert_element==False and "Li" in lines[i]:
                insert_element = True
                self.head_no = i

            if (insert_element == True):
                file_data = lines[i].split()
                element= str(file_data[0]).rstrip()

                mat1= re.search (r'(?P<var>[A-z]+)[0-9]+.*',element)
                m= mat1.group('var')
                #print (m)
                if m== 'Li':
                    self.num_Li+=1

                    if self.num_Li in self.list_2_ren:
                        element = self.n_name
                        file_data[len(file_data)-1] = self.n_name

                    others = ''
                    for i in range(1,len(file_data)):
                        others = others + '  ' + file_data[i]
                    others = others + '\n'

                    self.Li_info[self.num_Li]= dict()
                    self.Li_info[self.num_Li]['element']= element
                    self.Li_info[self.num_Li]['other']= others
                else:
                    others = ''
                    for i in range(1,len(file_data)):
                        others = others + '  ' + file_data[i]
                    others = others + '\n'
                    self.num_otherelements+=1
                    self.otherelements_info[self.num_otherelements]= dict()
                    self.otherelements_info[self.num_otherelements]['element']= element
                    self.otherelements_info[self.num_otherelements]['other']= others

def _filter(self, x):
    for i in self.list_2_rem:
        #print()
        if (x==i):
            return 1
    return 0
```

```
    def Li_struc(self, x):
        """Returns the declarations of the Li elements"""
        return (self.Li_info[x]['element']) +'  ' + (self.Li_info[x]['other'])

    def otherelements_struc(self,x):
        """Returns the declarations of the other elements"""
        return (self.otherelements_info[x]['element']) +'  ' + (self.otherelements_info[x]['other'])

    def generate_file(self):
        """write the final file to the output file"""
        with open(self.input_file, 'r') as input_file:
            with open(self.outfile, 'w') as out_file:
                i=0
                lines = input_file.readlines()
    #               print(len(lines))
                while i < self.head_no:
                    out_file.write(lines[i])
                    i=i+1
                for x in range (1, self.num_Li+1):
                    if(self._filter(x)==0):
                        out_file.write(self.Li_struc(x))

                for x in range (1, self.num_otherelements+1):
                    out_file.write(self.otherelements_struc(x))
```

C.6.2. Run File

```
"""Main script used to generate, run, and record execution time of smt2 proofs"""

import os
if not os.path.exists('output'):
    os.makedirs('output')

import sys
import time
#from time import sleep
import itertools as it

from main import _generator


start = time.time()
file_num = 1
def main():
    """Main function"""
    global file_num
```

```
print ('Assuming main file: mother_file.cif')
print ('Searching for the number of Li in mother_file')
li_count = 0
with open('mother_file.cif', 'r') as input_file:
        lines = input_file.readlines()
        for i in range(1,len(lines)):
            file_data = str(lines[i]).split()
            if file_data:
                if 'Li' in file_data[0]:
                    li_count = li_count + 1
print('Total number of Li found: ',li_count)

_no = int(input('Enter the number of Li to be eliminated: '))
#print('Removing 4 Li at a time...')
print('Generating removal list...')
removal_list = list(it.combinations(range(1,li_count+1),_no))

_rm = int(input('Enter the number of Li to be renamed: '))
#print('Renaming 2 Li at a time...')
print('Generating rename list...')
rename_list = list(it.combinations(range(1,li_count+1),_rm))

_nm = str(input('Enter the substitute name: '))
_no_file = int(input('Enter the no of output file: '))

print('Creating files...')
print('Cross checking if remove list and rename list have common index...')

for i in range(0, len(removal_list)):
    rename_index = 0
    for j in range (0,len(rename_list)):
        if set(removal_list[i]).isdisjoint(rename_list[j]): #not any(k in removal_list[i] for l in
rename_list[j]):
            rename_index = j
            #print(rename_list[j],removal_list[i])
            break

    Object                                =                                _generator('mother_file.cif',
'output/'+'output'+str(file_num)+'.cif',removal_list[i],rename_list[rename_index],_nm)
    Object.generate_file()
    file_num = file_num + 1
    rename_list.pop(rename_index)

    if(file_num>_no_file):
        break
print('Done creating files...')
```

```
if __name__ == '__main__':
    main()

end = time.time()

#print(end-start)
```